# Investigating muscle function in children with foot deformities due to cerebral palsy

## Development and application of a personalized musculoskeletal foot model

MSc. Thesis

Gaia van den Heuvel

TU Delft

Amsterdam UMC

# Investigating muscle function in children with foot deformities due to cerebral palsy

## Development and application of a personalized musculoskeletal foot model

by

Gaia van den Heuvel

to obtain the degree of Master of Science in Biomedical Engineering
at the Delft University of Technology,
to be defended publicly on Monday March 27, 2023.


| | | |
|---|---|---|
| Student number: | 5174732 | |
| Supervisors: | Dr. ir. A. Seth | TU Delft |
| | Dr. M. M. van der Krogt | Amsterdam UMC |
| | Dr. W. Schallig | Amsterdam UMC |
| Thesis committee : | Dr. M. G. H. Wesseling | TU Delft |


An electronic version of this thesis is available at http://repository.tudelft.nl/.

Cover: photo by Anne Nygård on Unsplash

TU Delft

# Table of contents

# Abstract

Children with cerebral palsy (CP) commonly have bony deformities of the foot, which lead to pain and gait problems. One of the causes of such a deformity is an imbalance in muscle forces around the foot. In turn, the bony deformity can also alter muscle function, due to, for example, altered muscle moment arm lengths. In this study, the altered muscle function due to hindfoot varus deformities in children with CP was investigated using musculoskeletal models. The first aim of this study was to create personalized musculoskeletal models of the foot based on weight-bearing computed tomography (WBCT) data. Secondly, we applied the model to get insight in how joint axis orientations and muscle moment arms are altered in varus feet, and how this leads to differences in muscle function during gait.

Models were created in OpenSim for seven children with a hindfoot varus deformity due to CP, and four adults with neutral feet. Each model was based on WBCT scans and included five degrees of freedom in the foot (talocrural, subtalar, Chopart, Lisfranc and metatarsophalangeal joints). The orientations of the foot joint axes and moment arms of the extrinsic foot muscles were calculated. Subsequently, the models were combined with motion capture and ground reaction force data to calculate muscle activations during gait.

The joint axis orientations showed greater variability in the group of children with CP compared to the control group; in most subjects, changes in axis orientation were observed that may lead to a more rigid foot. Furthermore, the dorsiflexion moment arm of the tibialis anterior decreased, while the inversion moment arm increased; thus, the tibialis anterior became an even more effective invertor when a varus deformity of the foot was present. On the other hand, the eversion moment arms of the peroneal muscles tended to become smaller, meaning they would be less effective in resisting the varus deformity. Static Optimization results showed decreased activity in the tibialis muscles, and increased activity in the peroneal muscles. This increased activity might be necessary due to the smaller moment arms, and/or to stabilize the ankle.

This is the first study in which a musculoskeletal foot model was developed based on personalized bone data of feet with bony deformities in weight-bearing conditions. Distinct changes were shown in muscle function when a varus deformity is present, which might lead to progression of the deformity. This contributes to a better understanding of the altered muscle function due to foot deformities, which may eventually contribute to improvement of treatment to prevent the progression of foot deformities.

# List of Figures

# List of Tables

# Acknowledgements

First and foremost, I want to thank my supervisors dr. Ajay Seth, dr. Marjolein van der Krogt and dr. Wouter Schallig. Ajay, thank you for challenging me to get the most out of this project and providing me guidance through the challenges of musculoskeletal modeling whenever I needed it. Marjolein, I appreciate your critical eye and your ideas and suggestions throughout the project. Wouter, thank you for always being open to discussions and questions; I appreciate your enthusiasm and advice along the way.

I would also like to thank dr. Ruud Wellenberg, for providing me with the CT data and helping me out with all the questions I had about it.

After having had to work from home during most of my master's, it's been certainly nice to be able to work on location at both the TU Delft and VUmc during my thesis project. I've met many people in the past year and I've learned a lot from everyone. Especially the group in the students' room at the VUmc: I've really enjoyed working together, sharing experiences and ideas, and not to mention the cake-days and many lunch walks!

Finally, last but definitely not least, my parents and Willem – thank you for your never-ending support, advice, and encouragement. It means a lot to me.

# Abbreviations

| | |
|---|---|
| **AFM** | Amsterdam Foot Model |
| **CAST** | Calibrated Anatomical System Technique |
| **CGA** | clinical gait analysis |
| **CP** | cerebral palsy |
| **CT** | computed tomography |
| **EMG** | electromyography |
| **FPI** | Foot Posture Index |
| **GMFCS** | Gross Motor Function Classification Score |
| **GRF** | ground reaction force |
| **HBM** | Human Body Model |
| **MRI** | magnetic resonance imaging |
| **MTP** | metatarsophalangeal |
| **WBCT** | weight-bearing computed tomography |

# 1 Introduction

Of every 1000 children born worldwide, between 1.5 and 3 are born with cerebral palsy (CP) (Sadowska et al., 2020). This disorder, caused by injury to the brain around the time of birth, leads to motor impairments – for example, muscle weakness, spasticity or dystonia (Aisen et al., 2011). Abnormal postural support and muscle tone may in time lead to abnormal bone development, such as hip dislocation, torsional deformities of the femur and tibia, and foot deformities (Gormley, 2001). It has been estimated that 93% of children with CP will develop a bony deformity of the foot (O'Connell et al., 1998). These deformities can have severe consequences, like pain, issues with fitting of shoes and orthoses, and gait problems (Davids, 2010).

A foot deformity is characterized by abnormal relative bone positions and orientations (Ledoux et al., 2006; Wellenberg et al., 2022). The type of foot deformity can be described by the position of the different parts of the foot, such as an equinus position of the ankle, varus or valgus position of the hindfoot, and cavus or planus position of the midfoot (Kedem & Scher, 2015). Two types of deformity commonly associated with hindfoot varus (an inverted orientation of the calcaneus) are cavovarus and equinovarus (Figure 1.1). Cavovarus is characterized by a high medial arch in addition to the hindfoot varus (Lee & Sucato, 2008). The equinus component in a deformity is characterized by excessive plantar flexion in the ankle (Davids, 2010).

**Figure 1.1:** From left to right: a right foot with varus, cavus and equinovarus foot deformity.

Describing the causes and development of a foot deformity is challenging, as many factors are involved. Muscle imbalance, soft-tissue contractures, bony torsion and joint instability may all occur, while the child is also growing (Miller & Church, 2020). In hindfoot varus deformities, muscle imbalance between the

invertor and evertor muscles is considered an important factor in the development of the deformity (O'Connell et al., 1998). Furthermore, these foot deformities are progressive, due to persistent muscle imbalances, development of contractures and a progressive mismatch between muscle and bone length (Bloom & Sabharwal, 2022).

During gait, the foot provides a stable connection to the ground, and acts as a lever arm for the ground reaction force (GRF) (Miller, 2020). We can hypothesize that a foot deformity leads to altered muscle moment arm lengths around the joints, compromising the function of the muscles during gait. Current diagnostic methods to investigate muscle function are not able to distinguish between primary neurological impairments and secondary disturbances caused by the deformity (Blemker et al., 2007; Theologis, 2013).

In this study, the altered muscle function due to hindfoot varus deformities in children with CP was investigated using musculoskeletal models. These models are able to make a distinction between primary impairments and altered function due to the deformity, as they allow for the determination of variables that are not measurable *in vivo* and can be used to determine how elements of the musculoskeletal system interact with each other (Hicks et al., 2015; Reinbolt et al., 2011). Therefore, these models can provide insight in how muscle function is affected by the skeletal deformity, which can add to our understanding of gait abnormalities, and aid in treatment planning (Arnold & Delp, 2005).

In most studies that use musculoskeletal simulations, a generic model is used, which is scaled to match the dimensions of the subject. However, in the case of skeletal deformities, these generic models may not be sufficiently accurate, and subject-specific models based on imaging data might be necessary. Previous studies have shown differences in simulation results when comparing subject-specific models of participants with aberrant femoral and tibial bone geometry compared to scaled-generic models (Bosmans et al., 2014; Correa et al., 2011; Kainz et al., 2021; Wesseling et al., 2019). In these studies, geometrical bone shapes were based on magnetic resonance imaging (MRI) or computed tomography (CT) scans, obtained in a supine position.

More recently developed medical devices can provide three-dimensional weight-bearing computed tomography (WBCT) images, that can capture bone alignment under loading conditions with relatively low radiation doses (Leardini et al., 2019). Several studies have shown changes in foot bone alignment between non-weight-bearing and weight-bearing CT scans, in both normal and pathological feet (Broos et al., 2021; De Cesar Netto et al., 2017; Hirschmann et al., 2014).

In previous research, several musculoskeletal foot models have been developed (e.g. Maharaj et al., 2021; Malaquias et al., 2017; Prinold et al., 2016; Saraswat et al., 2010; Sikidar & Kalyanasundaram, 2022). Only one study developed personalized musculoskeletal models of the foot based on MRI data, which were used to study joint reaction forces related to Juvenile Idiopathic Arthritis (Prinold et al., 2016). However, to our knowledge, no personalized models have been made of feet with a deformity to study related muscle function. In addition, using WBCT imaging to create personalized musculoskeletal models of the foot would allow for simulations of gait based on bone geometry and alignment under more realistic loading conditions.

Therefore, the first aim of the current study was to create personalized musculoskeletal models of the foot based on WBCT data of both children with CP with varus foot deformities, and adults with neutral feet. Secondly, using these models, the following research questions were addressed:

I. What are the structural differences between neutral feet and feet with varus deformities due to CP, in terms of joint axes orientations and muscle moment arms?

II. How do these structural differences of varus feet lead to differences in muscle function during gait?

# 2
# Methods

## 2.1. Participants

Seven children with CP were included in this study (five male, two female; age [mean ± standard deviation] 14.1 ± 2.3 years; height 160.9 ± 13.2 cm; weight 50.6 ± 11.9 kg). All children had a severe hindfoot varus foot deformity and underwent clinical gait analysis (CGA) and a WBCT scan at Amsterdam UMC as part of clinical practice, prior to orthopaedic foot surgery. Most children received the CGA and WBCT within a month from each other, with a maximum of four months. Participant characteristics of this group are shown in Table 2.1. Included feet (five right feet, two left feet) are shown in bold. Only the foot with a varus deformity was included in the current study; if they had a varus deformity on both feet, the most affected foot was included, as defined by the most deviating Foot Posture Index (FPI) score. This measure of foot posture ranges from –12 to +12, where 0 to +5 is considered normal, ≥+6 is considered a pronated (valgus) foot and ≤–1 is considered a supinated (varus) foot (Redmond et al., 2008). In one patient, the FPI was not determined, and the most affected foot was determined based on visual inspection.

**Table 2.1:** Subject characteristics of the patient group.

| # | Left foot (FPI) | Right foot (FPI) | GMFCS | Uni-/bilateral |
|---|---|---|---|---|
| 01 | planovalgus (+5) | **equinovarus (–10)** | 1 | bilateral |
| 02 | cavovarus | **equinovarus** | 2 | bilateral |
| 03 | neutral (+3) | **equinovarus (–10)** | 1 | unilateral |
| 04 | planovalgus (+4) | **equinovarus (–10)** | 2 | bilateral |
| 05 | **cavovarus (–7)** | neutral (+1) | 1 | unilateral |
| 06 | cavovarus (–3) | **cavovarus (–5)** | 1 | bilateral |
| 07 | **equinovarus (-8)** | neutral (+2) | 3 | unilateral |

*Note:* Included feet are shown in bold text. *Abbreviations:* FPI = Foot Posture Index, GMFCS = Gross Motor Function Classification Scale.

Most children had a Gross Motor Function Classification Score (GMFCS) of I or II, meaning they were able to walk independently, without a hand-held mobility device (Carnahan et al., 2007). One had a GMFCS score of III, but walked without a mobility device during the CGA. None of the children had prior bony surgery to their foot, or recent (< 4 years) soft tissue surgery, like muscle-tendon lengthening.

In addition, the right feet of four non-affected adults were analyzed as a control group (age 37.8 ± 4.8 years; height 179.4 ± 5.0 cm; weight 80.3 ± 10.9 kg). All control subjects had a FPI within the normal range values (i.e. between 0 and +5, FPI 2.8 ±

0.96), no recent (< 3 months) foot or ankle injury, no history of trauma or surgery of the foot, and they did not wear insoles.

All participants (and/or their parents) signed informed consent for both the use of the gait analysis and WBCT data for research purposes. For the latter, either informed consent was signed, or the use of the data was not declined within four weeks via an objection procedure (Wellenberg et al., 2022). The requirement for ethical review of the study was waived under the Medical Research Involving Human Subjects Act by the local medical ethics committee of Amsterdam UMC.

## 2.2. Weight-bearing CT data collection

WBCT scans were made using a Planmed Verity cone-beam CT system (Planmed Oy, Helsinki, Finland). Participants stood in the scanner on one leg. If necessary, a physician fixated the knee to reduce motion (Wellenberg et al., 2022). Due to the limited field of view and scan height, only the foot was scanned, with a small part of the distal tibia/fibula. For the control subjects, separate hindfoot and forefoot images were made and subsequently stitched together (Broos et al., 2021). The middle and distal phalanges, except for the first distal phalanx, were not included in the scans. For the children with CP, only scans of the hindfoot and midfoot (up to and including the metatarsals) were made. The bones were semi-automatically segmented using Disior (Disior Oy, Helsinki, Finland).

## 2.3. Musculoskeletal foot model development

A personalized musculoskeletal model of the foot was created for each subject in OpenSim Creator (version 0.3.0) (Kewley, 2023). The rationale behind all aspects of the model is explained in the following sections.

### 2.3.1. Segment definitions

We developed a foot model with five segments: talus, calcaneus, midfoot (cuboid, navicular and cuneiform bones), forefoot (metatarsals) and toes (phalanges), as shown in Figure 2.1. As such, this multi-segment foot model is able to capture the motion of not only the ankle, but also the motion within the intrinsic joints of the foot, see Figure 2.2. This is important, because it has been shown that there is considerable motion in these joints (Leardini et al., 2007), and they contribute to power absorption and generation during gait (Deschamps et al., 2017). In consequence, single-segment foot models have been shown to lead to inaccuracies in measured ankle joint motion and power, and overestimate muscle lengths, especially in pathological gait (Eerdekens et al., 2019; Pothrat et al., 2015; Zandbergen et al., 2020). Including the intrinsic foot joints in the model also allows insight into the functioning of these joints during gait, which is considered important by clinical experts (Schallig et al., 2022).

Each segment has a fixed body reference frame, with the origin at the joint center (described below) (Malaquias et al., 2017). The body frames were oriented such that in neutral position the body reference frames were aligned with the OpenSim reference coordinate system (i.e. x-direction anterior, y-direction superior and z-direction to the right).

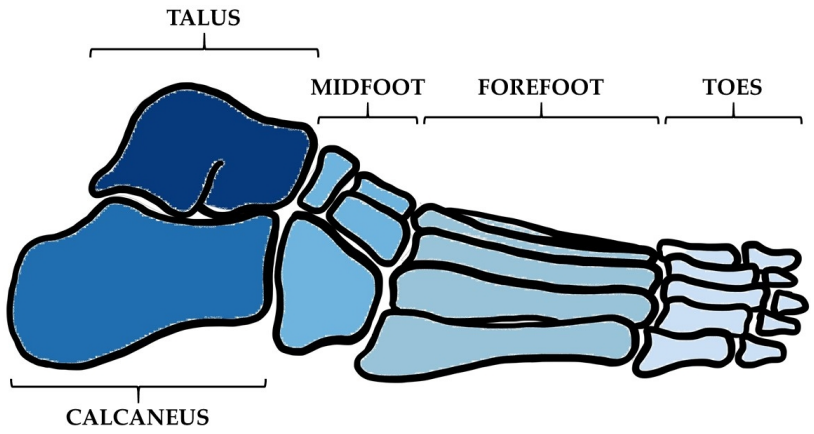


**Figure 2.1:** Segment definitions of the foot model.

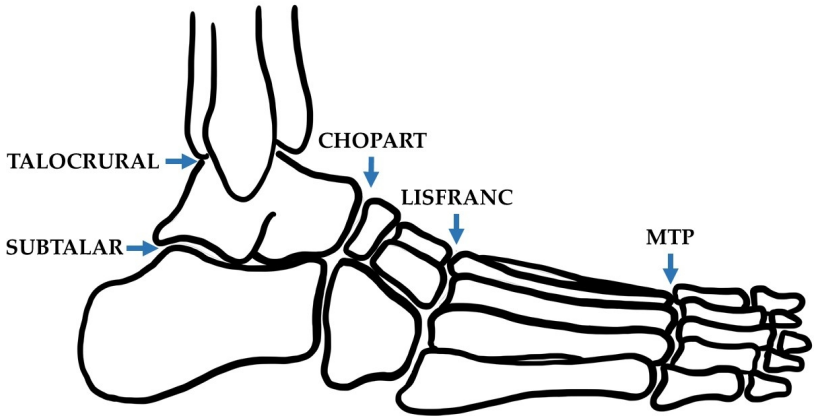


**Figure 2.2:** Joints in the foot model.

The phalanges of the children with CP were not included in the CT images. Therefore, the meshes of the phalanges of one of the control subjects were added to the foot models of the children. In most cases, they were slightly scaled (based on visual inspection) to match with the foot size of the children, and then each was manually placed and oriented based on the metatarsals and photos taken of the feet.

### 2.3.2. Joint axis definitions

The positions and orientations of the joint axes are important considerations in a model: the orientation of an axis determines the relative proportions of motion in the three planes, whereas the orientation and position both influence the moment arms of the forces (e.g. muscle forces, ground reaction forces) at the joint (Nester, 1998). In the various foot models previously published (e.g. Maharaj et al., 2021; Malaquias et al., 2017; Prinold et al., 2016; Saraswat et al., 2010; Sikidar & Kalyanasundaram, 2022), different definitions for the foot joint models have been used. By definition, the joint axes in the model will be a simplification of the true physiological joint axes. Especially the axes of the intrinsic joints of the foot are often complex, and in some cases there is no consensus yet on the physiological joint mechanism. What adds to the complexity, is that there seems to be considerable variation in joint axis orientation between individuals (e.g. Isman & Inman, 1969; Lundberg & Svensson, 1993; Nester, 1997). Joint axis orientations are regularly reported as average angles

relative to the anatomical planes; in Maharaj et al. (2021), for example, such average angles were adopted to define the joint axes. In the case of foot deformities, however, average angles might not suffice. In addition, the purpose of this model is to emphasize individual variation in bone geometry. For this reason, we chose to define the orientations of the joint axes based on anatomical landmarks. These landmarks, in turn, are based on literature with slight adjustments to fit the model and for reproducibility. All joints were modeled as hinge joints. An overview of the joint axis definitions and locations of the anatomical landmarks is given in Table 2.2 and explained below.

**Table 2.2:** Overview of joint axis definitions.

| Joint | JRC | Anatomical landmark 1 | Anatomical landmark 2 |
|---|---|---|---|
| Talocrural | Midpoint between the two anatomical landmarks | Immediately distal to the tip of the tibial malleolus (on the talus) | Below the distal end of the anterior curve of the fibular malleolus, at a height immediately distal to the tip of the malleolus (on the talus) |
| Subtalar | The point on the joint axis at the height of the upper edge of the sustentaculum tali | Midpoint of the narrowest part of the superior surface of the talar neck | Posterolateral inferior point of the calcaneus |
| Chopart | Midpoint between (1) medial medium point of the talonavicular articulation (on the navicular), and (2) lateral medium point of the calcaneocuboid articulation (on the cuboid) | JRC | Lateral process of calcaneal tuberosity |
| Lisfranc | Midpoint between (1) medial medium point of the first MT-medial cuneiforme articulation (on the first MT), and (2) lateral tuberosity of the fifth MT | Navicular tuberosity | Superior surface of the base of the third MT |
| MTP | Midpoint between the two anatomical landmarks | Medium point of the medial edge of the articular surface between the first MT and the first proximal phalanx (on the first MT) | Medium point of the lateral edge of the articular surface between the fifth MT and the fifth proximal phalanx (on the fifth MT) |

*Abbreviations*: JRC = joint rotation center; MTP = metatarsophalangeal, MT = metatarsal.

### Talocrural joint

The talocrural joint is primarily responsible for ankle plantarflexion-dorsiflexion motion, and has an oblique axis relative to the anatomical planes. Similar to Delp et al. (1990), the talocrural joint axis was defined in the current model based on the cadaver measurements of Isman and Inman (1969). This approximates the talocrural joint as a hinge joint, running distal to the tips of the tibial and fibular malleoli.

Isman and Inman (1969) located the axis on the lateral end a little anterior and distal to the tip of the fibular malleolus, and on the medial end a little distal to the tip of the tibial malleolus. We slightly shifted these landmarks: on the medial side directly below the tip of the tibial malleolus on the talus, and on the lateral side below the anterior curve of the fibular malleolus, at the height of the distal tip of the malleolus. Being closer to these anatomical points (i.e. the tips of the malleoli) ensures that the landmarks can be placed more accurately and consistently. The joint rotation center was then defined as the midpoint of this line (Lundberg et al., 1989).

**Subtalar joint**

The motion at the subtalar joint is described as a combination of inversion-eversion, adduction-abduction and plantarflexion-dorsiflexion. It is generally established that the subtalar joint axis runs from posterior-lateral-inferior to anterior-medial-superior, anteriorly piercing the talus at the superior aspect of the talar neck (Kirby, 2001). This was also confirmed by more recent research using WBCT scans evaluating the helical axis of this joint (Peña Fernández et al., 2020). This same study also showed the joint rotation center is located between the middle and posterior facets of the subtalar joint, i.e. around the sustentaculum tali.

We defined the subtalar joint axis as running from the lower lateral "corner" of the posterior side of the calcaneus to the center of the superior surface of the talar neck, identified using the images presented in the works of Nozaki et al. (2017) and Peña Fernández et al. (2020). The joint rotation center was then defined as the point along the axis at the height of the sustentaculum tali.

**Chopart joint**

Anatomically, the Chopart (midtarsal or transverse tarsal) joint is an S-shaped joint consisting of two articulations, the calcaneocuboid and talonavicular joint, that are commonly functionally grouped as a single joint. In the literature, there is controversy on how to model the axes of this joint. Commonly, a dual axis model with a longitudinal and oblique axis with simultaneous motion around both axes has been proposed to explain clinical observations, but there is no reliable experimental evidence (Tweed et al., 2008). A single oblique axis was therefore suggested to describe the function of the Chopart joint (Nester et al., 2001). However, no exact anatomical landmarks were specified to determine the axis orientation. Other authors also suggest that motion of this joint is much more complex, with an infinite number of motions being possible.

The joint rotation center was defined as the center of the midtarsal joint; the midpoint between the medial medium point of the articulation between the talus and the navicular, and the lateral medium point of the articulation between the calcaneus and the cuboid (Malaquias et al., 2017). The joint axis was subsequently modeled as passing through this joint center and the lateral process of the calcaneal tuberosity. This is a well-identifiable landmark between the positions of the longitudinal and oblique axes identified by Hicks (1953), and corresponds approximately to the (assumed anatomical position of the) average midtarsal joint axis presented in Nester et al. (2001).

#### Lisfranc joint

The Lisfranc (tarsometatarsal) joint is an articulation between many bones: the five metatarsals with the three cuneiform bones and the cuboid bone. The function of this joint is generally described by three columns: the medial column (first tarsometatarsal joint), central column (second and third tarsometatarsal joints), and the lateral column (fourth and fifth metatarsal joints). In the central column, however, there is minimal movement. Hicks (1953) has described the function of the Lisfranc joint as two joints: the first and fifth ray joint. The first ray allows a combined motion of flexion-pronation/extension-supination, whereas the fifth ray allows a combined motion of flexion-supination/extension-pronation. This was also adopted in the model published by Malaquias et al. (2017).

In the current model, only the first ray axis as defined by Hicks (1953) was used. The joint rotation center was defined as the midpoint between the medial medium point of the articulation between the cuneiform and first metatarsal, and the lateral tuberosity of the fifth metatarsal (Malaquias et al., 2017). The orientation of the first ray axis was defined by the base of the third metatarsal and the position of the navicular tuberosity (Hicks, 1953). So the axis runs parallel to this line, through the joint rotation center.

#### Metatarsophalangeal joint

Once again, there is no consensus on the exact definition of the metatarsophalangeal (MTP) joint axis, which connects the forefoot (metatarsals) with the phalangeal bones of the toes. Although a more anatomically correct axis would be a dual axis around the first and second metatarsals and the second to fifth metatarsals, the joint is commonly modeled as a single oblique axis with the joint center at the midpoint between these locations (Day & Hahn, 2019). The position of this axis is often defined by the first and fifth metatarsal heads, but it has been shown that the functional axis of the joint is more anterior and superior (Raychoudhury et al., 2014). Therefore, we defined the MTP joint axis from the medial medium point of the articulation between the first metatarsal and first proximal phalanx, and the lateral medium point of the articulation the fifth metatarsal and the fifth proximal phalanx, with the joint rotation center defined as the midpoint between these two landmarks. This is similar to the MTP joint rotation center in the model defined by Malaquias et al. (2017).

### 2.3.3. Body segment parameters

The inertial parameters of the foot segments (mass, center of mass and inertia tensor) were estimated based on the available experimental data, and calculated using MATLAB (R2022b; The MathWorks, Inc., Natick, USA).

#### Mass

The total foot mass was calculated as 1.4% of the total body mass (Dempster, 1955). The relative masses of the segments were subsequently calculated based on the bone volume distribution of the CT scans. Hence, a uniform mass distribution was assumed, with no influence of the soft tissues on the mass distribution.

As (part of) the phalanges were missing in the CT scans, the volume of the toes was calculated as 1/3.17 the volume of the forefoot (metatarsals). This was based on the average ratio between metatarsal and phalanges volume in Pietak et al. (2013).

#### Center of mass

The center of mass was approximated by the centroid of the segment. Again, a uniform mass distribution was assumed, with no influence of the soft tissues on the mass distribution.

The centroids of the toes segments of the children with CP were not known due to these bones not being scanned, and the centroid of the toes segment of the control subject was not accurate anymore for these children due to the individual phalanges being repositioned. Therefore, the function in OpenSim Creator to place a point ("station") at the bounds center (the center of the bounding box, i.e. the smallest box that contains all mesh vertices) of the third digit was used, and the coordinates of this point were subsequently used as the coordinates of the center of mass.

#### Inertia tensor

The moments of inertia about the mass center were calculated by modeling each segment as a geometric solid with uniform density, that resembles the segment as closely as possible. The talus was modeled as a cuboid shape; the calcaneus as a circular cylinder; and the midfoot, forefoot and toes as elliptical cylinders. The dimensions of the segments were calculated based on (averaged) marker positions in the static trial (see section 2.4). These calculations are further outlined in Appendix A.

### 2.3.4. Full body model and muscle geometry

The personalized foot that was created was attached to the full-body *Gait2392* model (Anderson & Pandy, 1999, 2001; Delp et al., 1990; Yamaguchi & Zajac, 1989) that is distributed with OpenSim (Delp et al., 2007; Seth et al., 2018). So, the final model consisted of a generic model scaled to the dimensions of the participant, with a subject-specific foot. This full body model contains 92 muscles, including the eleven extrinsic muscles of the foot that originate from the lower leg and insert on the foot bones. In an OpenSim model, each muscle is represented by a single line of action, with the path defined by a series of attachment points on the bodies. On the foot, these are all fixed attachment points connected by straight lines.

#### Tibial torsion

As WBCT data was only available of the foot bones and a small part of the distal tibia, the orientation of the talocrural joint axis was defined based on the personalized tibia, but the tibial and fibular bones in the full-body model were those of the generic *Gait2392* model. However, the children included in this study also had an increased tibial torsion angle. Therefore, tibial torsion was added to the model to not only improve visualization of the connection between shank and talus, but also to rotate the muscle attachments on the tibia, which influences the moment arms of the muscles. Torsion was included for both children with CP and control subjects, only on the side of the personalized foot.

Tibial torsion was included using the Torsion Tool (Veerkamp et al., 2021). This MATLAB-based tool divides the mesh file of the tibia into three segments and rotates the distal third by the entire torsional angle, and the middle third with a linear increasing angle. The proximal third does not rotate. The muscle attachments rotate along with the tibia. As only the tibia is rotated in the Torsion Tool and not the

fibula, the code was extended to also include rotation of the fibula similar to the tibia for visualization purposes.

Tibial torsion angle can be measured as the angle between the transepicondylar axis and the transverse axis through the lower end of the tibia (Jakob et al., 1980). In this case, individual torsion angles were calculated as the angle between a line through the (experimental) markers on the epicondyles of the knee, and a line through the markers on the malleoli. In the Torsion Tool, the torsion angle of the generic *Gait2392* tibia is considered 0°. Therefore, the tibial torsion in the model was calculated at -9.25° (external rotation) using the aforementioned markers virtually placed on the model. This was seen as the "offset" and subtracted from the individually calculated tibial torsion angles.

### Muscle attachments

The muscle via points and insertions on the foot were manually moved to the correct location on the bone meshes. The same locations on the bone were used as in the *Gait2392* model; this was matched as closely as possible based on visual inspection. Table 2.3 lists the muscles in the model that attach on the foot.

**Table 2.3:** Foot muscles in the model, grouped by function (Schünke et al., 2016).

| Muscle | (Foot) motion | Insertion point |
|---|---|---|
| m. tibialis anterior | dorsiflexion; inversion/supination | medial and plantar surface of medial cuneiforme; medial basis first metatarsal |
| m. extensor hallucis longus | dorsiflexion; inversion/eversion*; extension (MTP I) | base of distal phalanx of hallux |
| m. extensor digitorum longus | dorsiflexion; eversion/pronation; flexion (MTP II-V) | base of distal phalanges of digits II-V |
| m. peroneus tertius | dorsiflexion; eversion/pronation | base of fifth metatarsal |
| m. soleus | plantarflexion; inversion | tuber calcanei |
| m. gastrocnemius medialis | plantarflexion; inversion | tuber calcanei |
| m. gastrocnemius lateralis | plantarflexion; inversion | tuber calcanei |
| m. tibialis posterior | plantarflexion; inversion/supination | navicular tuberosity, cuneiform bones, base of second to fourth metatarsal |
| m. flexor digitorum longus | plantarflexion; inversion/supination; flexion (MTP II-V) | base of distal phalanges of digits II-V |
| m. flexor hallucis longus | plantarflexion; inversion/supination, flexion (MTP I) | base of distal phalanx of hallux |
| m. peroneus longus | plantarflexion; eversion/pronation | plantar surface of medial cuneiforme, base of first metatarsal |
| m. peroneus brevis | plantarflexion; eversion/pronation | tuberosity of fifth metatarsal |

(*) Dependent on initial position.

## 2.4. Gait analysis data collection

Marker trajectories, ground reaction forces and plantar pressure data of the subjects were collected during 3D gait analyses. Marker trajectories were recorded using a

motion capture system (Vicon motion systems ltd., Oxford, UK; 100 Hz).

Passive reflective markers were placed on the foot and lower leg according to the Amsterdam Foot Model (AFM) (see Appendix B; Schallig et al., 2022), and on the rest of the lower body and torso according to the Human Body Model (HBM) (Flux et al., 2020; Van den Bogert et al., 2013) or Calibrated Anatomical System Technique (CAST) marker sets (Cappozzo et al., 1995). First, a static trial was collected, after which the subjects were instructed to walk barefoot over a 10-meter walkway. Children with CP walked at a self-selected speed, while the control subjects were instructed to walk at 75% of their comfortable walking speed, to allow for proper comparison. The marker data was processed using Vicon Nexus software (version 2.11).

Total GRFs were simultaneously collected using a single force plate integrated in the walkway (OR6 series; Advanced Mechanical Technology, Inc., Watertown, USA; 500 Hz). A pressure plate (0.5m footscan plate; RSscan, Paal, Belgium; 4096 sensors of 7.62 x 5.08 cm; 500 Hz) was placed exactly on top of the force plate. Both the force plate and plantar pressure data were processed in the Footscan software (version 9). The pressure data was dynamically calibrated and corrected using the vertical force plate data. Trials were included in which only one foot was placed fully within the bounds of the pressure plate. The GRF data was filtered using a low-pass second order Butterworth filter with a cut-off frequency of 6 Hz. The total GRF was split into partial GRFs per segment, based on a vertical projection of the markers on the pressure plate (see Appendix C).

## 2.5. Simulations

### 2.5.1. Scaling

The full body model (except for the already personalized foot) was scaled to match the dimensions of the subject. Scaling was done using the Scale Tool in OpenSim (version 4.4) (Delp et al., 2007), based on the difference in the distance between the virtual markers on the model and the average distance between the experimental markers in the static trial. Before scaling and marker registration, virtual markers corresponding to the AFM were placed on the corresponding locations on the bone meshes for each participant.

In OpenSim, it is also possible to assign a coordinate and a weight to a joint, which is then matched during the scaling process. A coordinate of 0° was imposed on the Chopart and Lisfranc joints with a slight weight to improve the static pose.

Two muscle parameters that depend on the length of the muscle, optimal fiber length and tendon slack length, are (linearly) scaled as well during the scaling process. Moving the muscle insertions on the personalized bone geometry modified the muscle lengths. Therefore, these two parameters were pre-scaled based on the length difference of the muscles in the original model and the adjusted muscle insertions. The maximum isometric muscle force of each muscle remained equal between the non-scaled and scaled model.

### 2.5.2. Structural measures

Joint axis orientations were taken from the Euler rotations of the joint coordinate systems in OpenSim Creator, with the Z-axis being the rotational axis of the pin

joint. Subsequently, to facilitate visualization and interpretation, the angle of the projection of the unit vector representing the axis on the three planes, with the respective axis was calculated.

Muscle moment arms of the extrinsic foot muscles were calculated using OpenSim. Only the moment arms around the hindfoot joints (talocrural, subtalar, and Chopart) were analyzed, as they are most relevant to the hindfoot varus deformity. The moment arm of a muscle represents its "effectiveness" with which it can generate torque around the joint and is mechanically represented as the shortest or perpendicular distance from the line of action of the muscle to the joint rotation center. For muscles crossing multiple joints, the moment arm is calculated over the range of the joint of interest, while the other joints are held constant. In the case of a non-straight muscle path (which is the case for many of the foot muscles) OpenSim calculates muscle moment arms using generalized forces (Sherman et al., 2013). To account for height differences, the moment arms were normalized by tibia length, which was calculated as the distance between the malleoli and knee markers.

#### Statistics

Because of the small sample size, a non-parametric Mann-Whitney U test was used to assess differences in joint axis orientation and moment arms between the CP group and control group. Differences were considered statistically significant when $p < 0.05$. This analysis was done in MATLAB.

### 2.5.3. Dynamic simulations of gait

Joint kinematics and kinetics were estimated over the gait cycle using the Inverse Kinematics and Inverse Dynamics tool, respectively. OpenSim calculates inverse kinematics by solving a least-squares problem that minimizes differences between the virtual markers on the model and the experimental marker locations (Delp et al., 2007). To assess the validity of the model, marker errors were calculated as the root mean square distance between the virtual and experimental markers. Net joint torques producing the given movement were calculated by solving the equations of motion for these unknown forces; these results are shown in Appendix D.

For comparison of the kinematics, the inverse kinematics simulations were repeated for two representative children with CP and two adults, with the generic OpenSim *Gait2392* model, and with a personalized model with the same number of joints as the generic model (i.e. no Chopart and Lisfranc joints).

Subsequently, muscle forces during the gait cycle were calculated using the Static Optimization tool, which minimizes the sum of squared muscle activations. For the Static Optimization analysis, the Chopart, Lisfranc and MTP joints were locked. This was done because the ligaments of the foot and the intrinsic foot muscles were not included in the model, which would normally account for a large portion of the stiffness in the intrinsic foot joints.

For each simulation, three trials were simulated and subsequently averaged. All simulated data was cut to one stride with initial contact defined using the method of Zeni et al. (2008), and time-normalized.

# 3
# Results

One participant from the CP group was excluded from the analyses, except for the joint axis orientations, due to issues with scaling and a lack of GRF data. For another CP participant, only one trial with force data was available, therefore only one trial was simulated during inverse dynamics/Static Optimization.

## 3.1. Joint axis orientations

In Figure 3.1, the joint axis orientations are shown graphically, in the transverse, frontal and sagittal plane. Figure 3.2 represents the angle in each plane as box plots. For the frontal and sagittal plane (anterior and lateral view), these are the angles the axis makes with the ground; for the transverse plane (superior view), this is the angle with the global mediolateral axis. Positive angles are anti-clockwise.

In the transverse plane (superior view), all joints except for the MTP joint tended towards a larger angle in the CP group, so more towards the anteroposterior axis. The MTP joint in the CP group was more in line with the mediolateral axis. However, there was considerable variation and the differences were not significant. Only in the Lisfranc and MTP joint there was a significant difference ($p < .05$).

In the frontal plane (anterior view), the axes were angled towards a more vertical orientation, with a significant difference in the subtalar and Lisfranc joint ($p < .05$).

Finally, in the sagittal plane (lateral view), there was more variation in the inclination angle of the axis with the ground. Only in the Lisfranc joint there was a significantly larger inclination angle ($p < .05$). In the Chopart joint the inclination angle tended to be smaller than the control group in equinovarus feet, while the inclination angle was larger than the control group in the cavovarus feet.

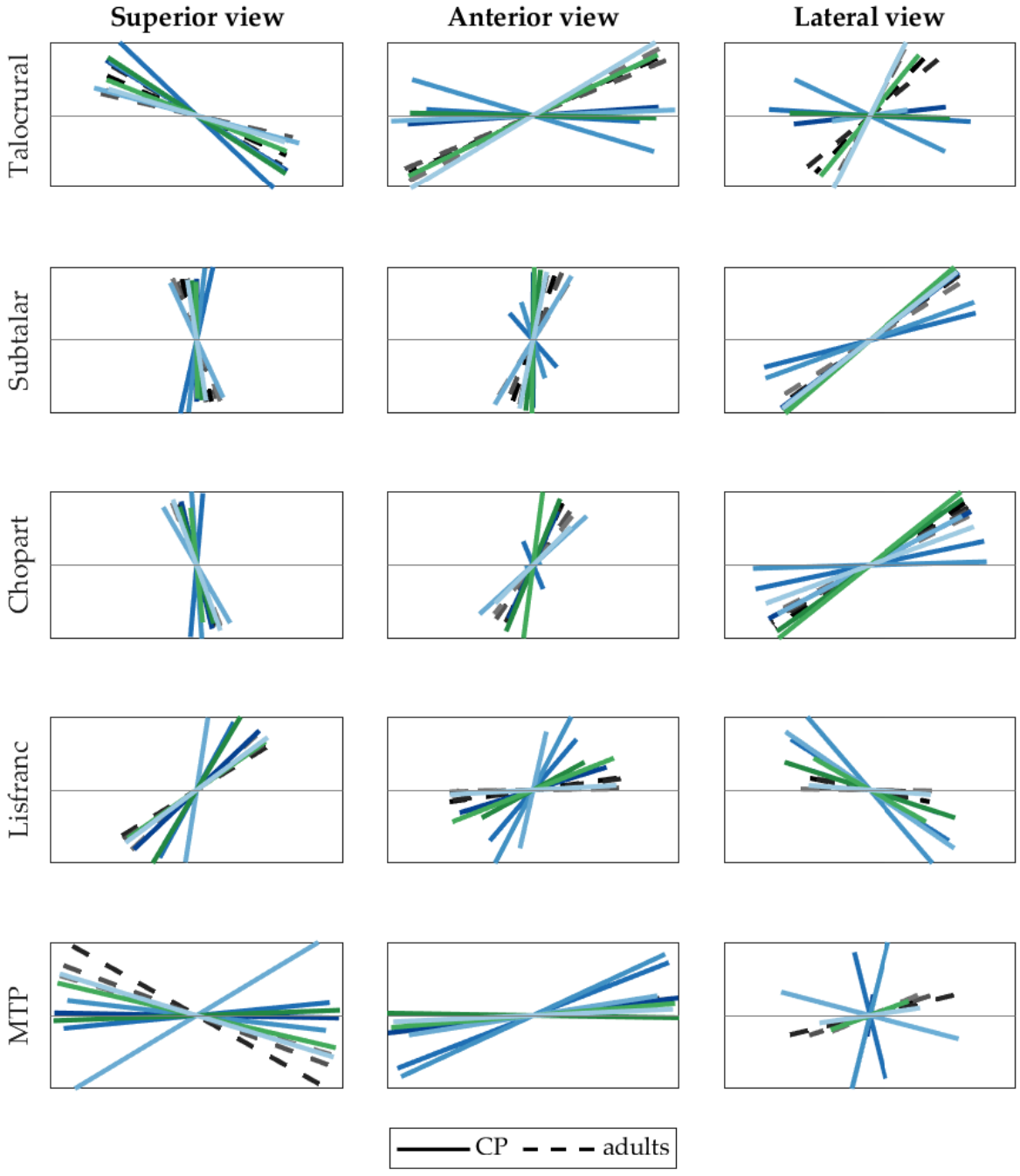


**Figure 3.1:** Visual representation of the joint axis orientations in the transverse (first column), frontal (second column) and sagittal plane (third column). Each line represents one subject. Children with a equinovarus deformity are represented with solid blue lines, while children with a cavovarus deformity are represented with solid green lines.

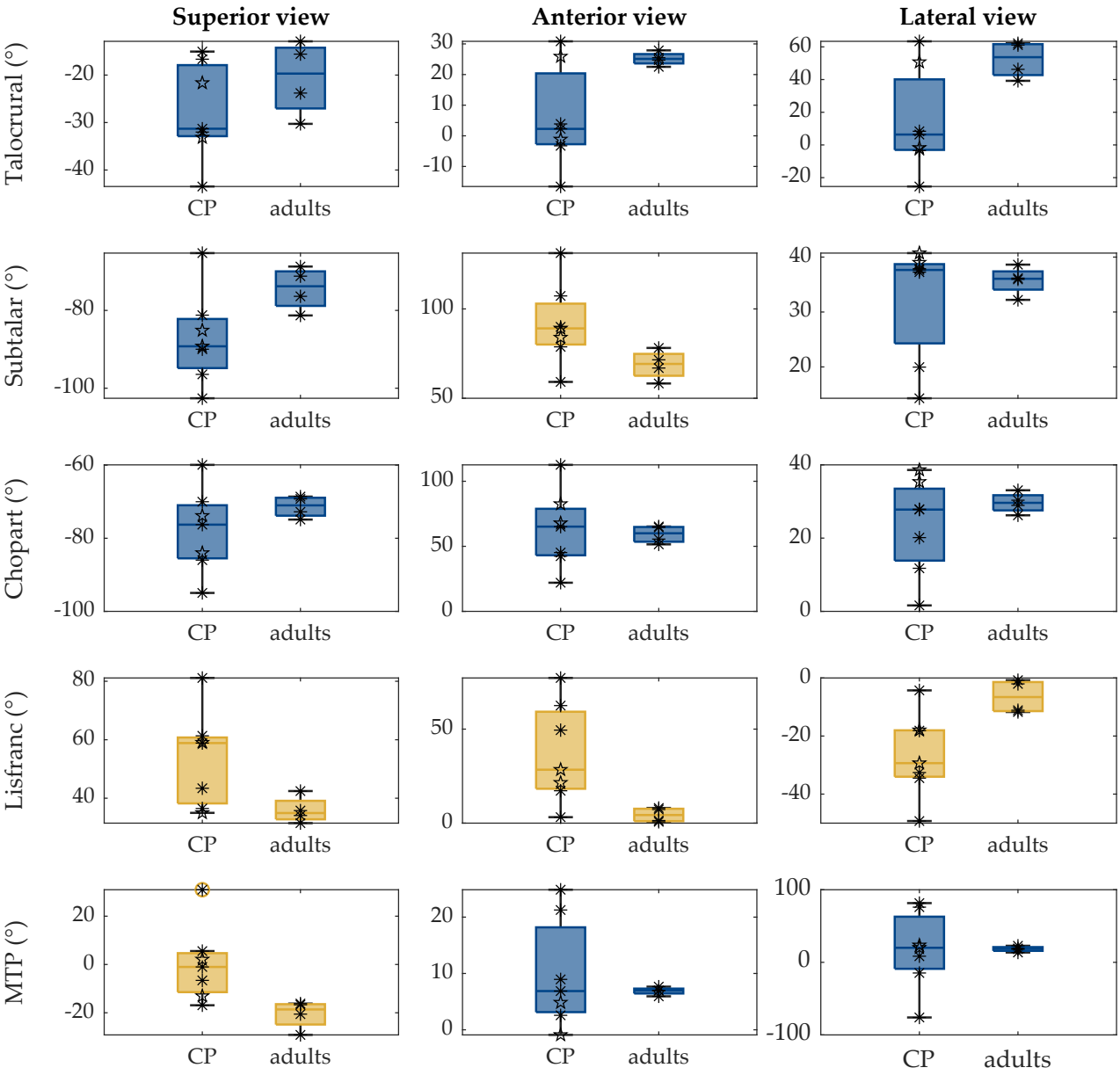


**Figure 3.2:** Box plots showing joint axes orientations in the transverse (first column), frontal (second column) and sagittal plane (third column). Yellow boxes indicate statistical significant differences between the groups. Individual data points are shown as asterisks on top of the boxes; the subjects with a cavovarus deformity are shown as pentagrams to differentiate them from the subjects with equinovarus.

## 3.2. Muscle moment arms

Figure 3.3 shows the plantarflexion-dorsiflexion moment arms of the muscles crossing the talocrural joint. The median dorsiflexion moment arm of both the tibialis anterior ($p < .01$) and extensor hallucis longus ($p < .05$) was significantly smaller in the CP group, with a decrease of 47.4% and 20.8%, respectively.

For the inversion-eversion moment arms around the subtalar joint (Figure 3.4), both the tibialis anterior and extensor hallucis longus again showed a significant difference, going from an eversion to an inversion moment arm ($p < .01$). The eversion moment arms of the peroneus tertius and extensor digitorum significantly

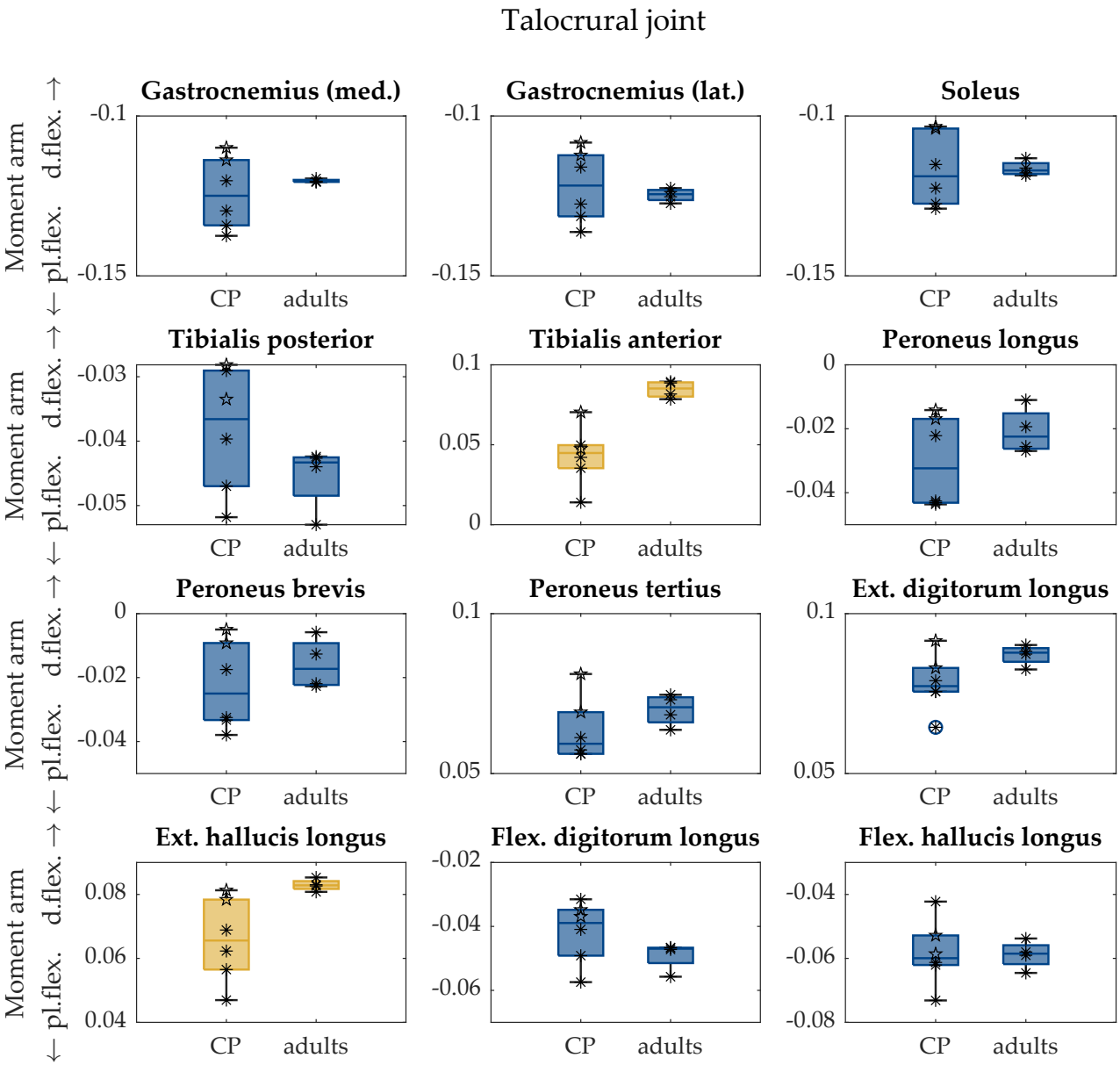


**Figure 3.3:** Normalized muscle moment arms around the talocrural joint. Yellow boxes indicate statistical significant differences between the groups. Individual data points are shown as asterisks on top of the boxes; the subjects with a cavovarus deformity are shown as pentagrams to differentiate them from the subjects with equinovarus.

decreased, with 41.8% and 46.3%, respectively ($p < .01$).

Around the Chopart joint, there were significantly different moment arms in the tibialis posterior, tibialis anterior, peroneus tertius, extensor digitorum longus and flexor digitorum longus. The median normalized supination moment arm of the tibialis anterior increased three times ($p < .01$), but on the other hand the supination moment arm of the tibialis posterior ($p < .01$) and flexor digitorum longus ($p < .05$) both decreased with 40%. The pronation moment arms of the peroneus tertius and extensor digitorum longus also decreased, with 34.3% ($p < .01$) and 34.9% ($p < .01$), respectively.

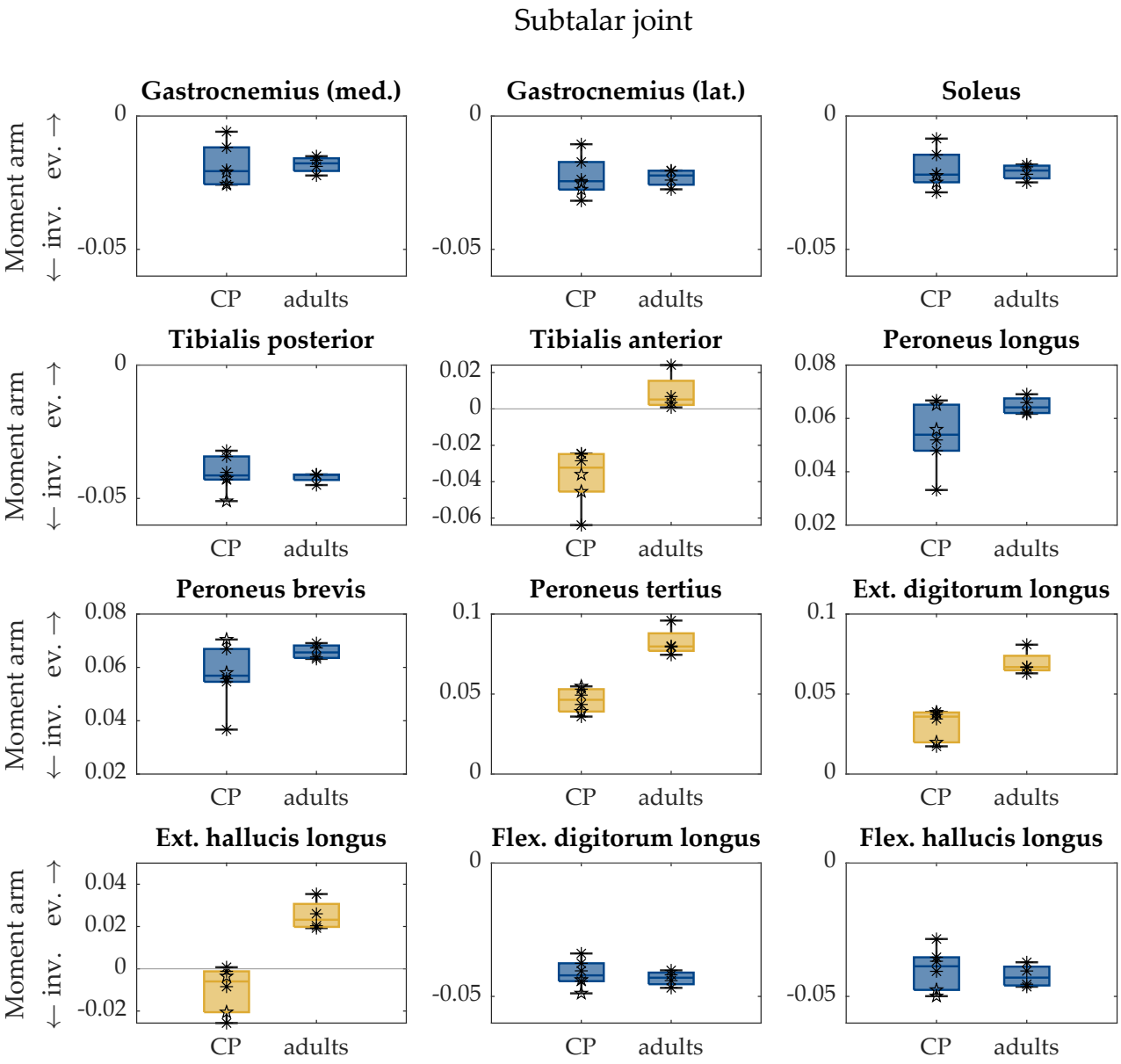


**Figure 3.4:** Normalized muscle moment arms around the subtalar joint. Yellow boxes indicate statistical significant differences between the groups. Individual data points are shown as asterisks on top of the boxes; the subjects with a cavovarus deformity are shown as pentagrams to differentiate them from the subjects with equinovarus.

## 3.3. Simulations of gait

Figure 3.6 shows the joint angles per subject during the gait cycle, while Figure 3.7 visualizes the average (foot) marker errors during these simulations. Maximum marker errors were around 0.9 cm.

When comparing the three different models, as depicted in Figure 3.8, we see slight differences between the foot model with and without midfoot joints, and larger differences in the generic model. This is especially evident for the subtalar joint and the two subjects with a varus deformity. Although all marker errors can be considered small, we do see slightly larger error in the foot model without a midfoot, and even larger errors in the generic model (Figure 3.9).

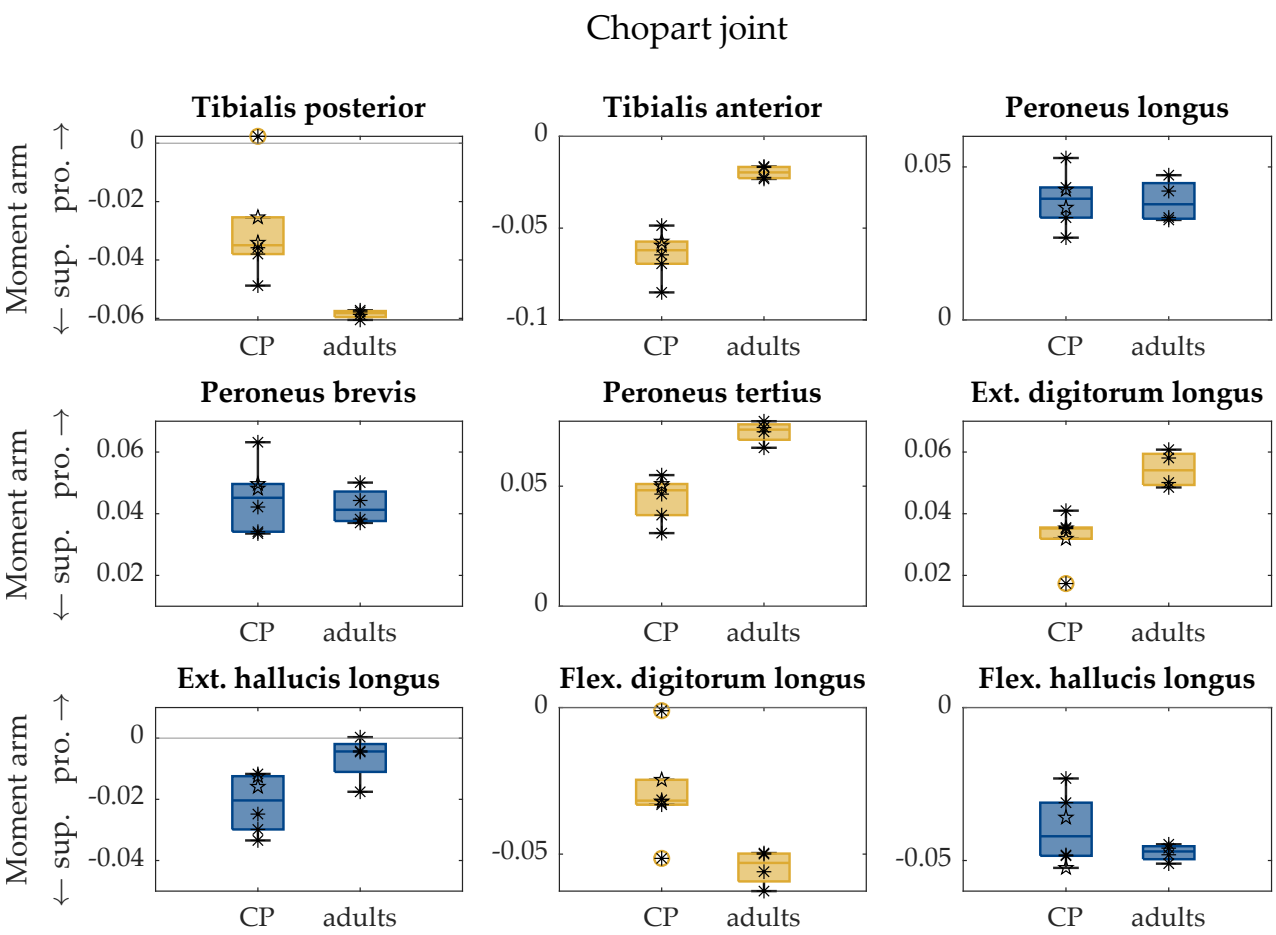


**Figure 3.5:** Normalized muscle moment arms around the Chopart joint. Yellow boxes indicate statistical significant differences between the groups. Individual data points are shown as asterisks on top of the boxes; the subjects with a cavovarus deformity are shown as pentagrams to differentiate them from the subjects with equinovarus.

Finally, calculated muscle activations during the gait cycle – without motion in the midfoot and MTP joints – are visualized in Figure 3.10. The triceps surae show activity already at initial contact in the CP group, whereas they only become active halfway through stance in the control group. During push off, the activation of the calf muscles is decreased, even more in the equinovarus group compared to the participants with cavovarus. We see much lower activity of the tibialis muscles (invertors), and much higher activity in the peroneal muscles (evertors) throughout the gait cycle in the CP group.

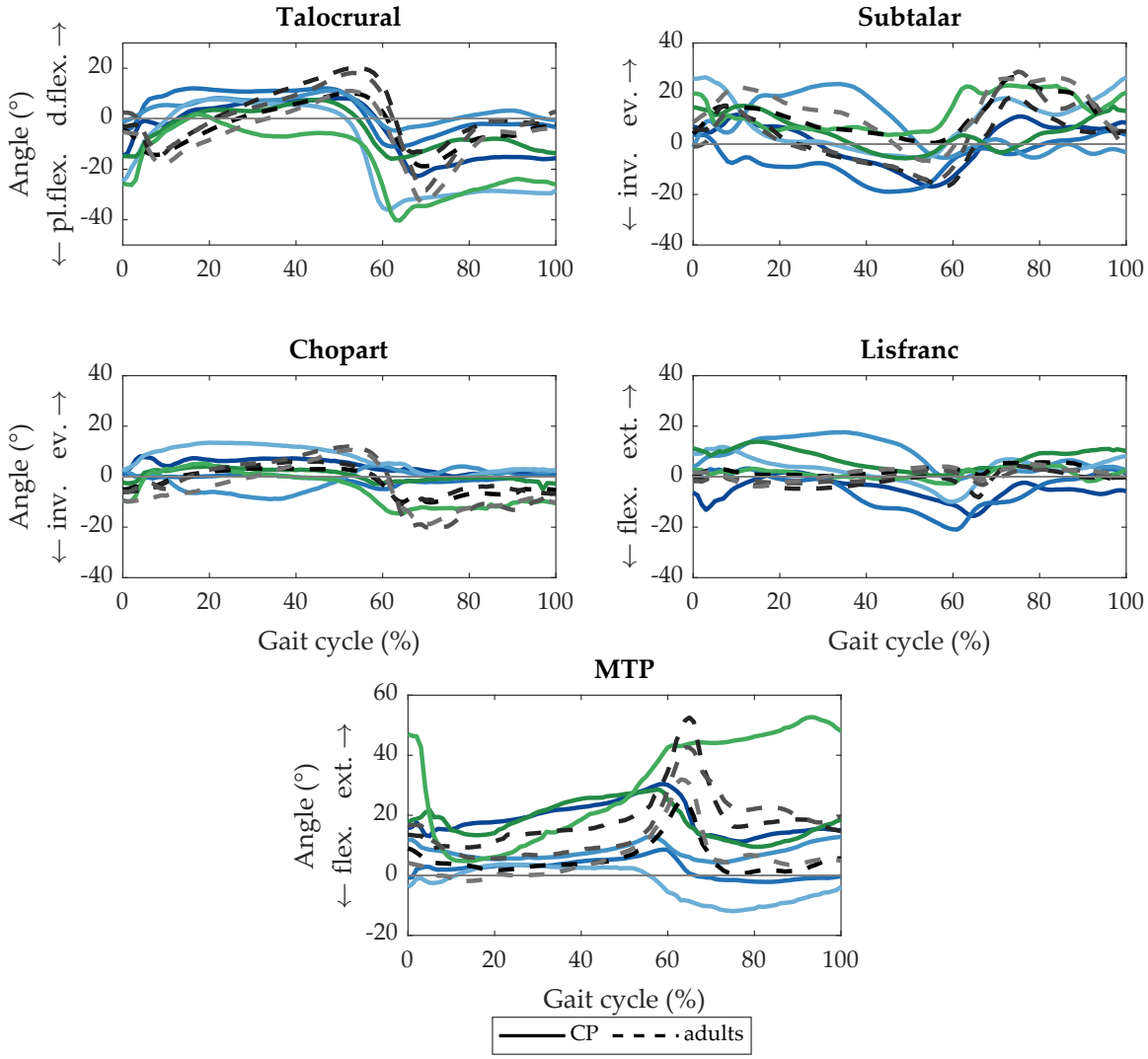


**Figure 3.6:** Inverse kinematics results: foot joint angles per subject, averaged over three trials. Each line represents one subject. Children with an equinovarus deformity are represented with solid blue lines, while children with a cavovarus deformity are represented with solid green lines.

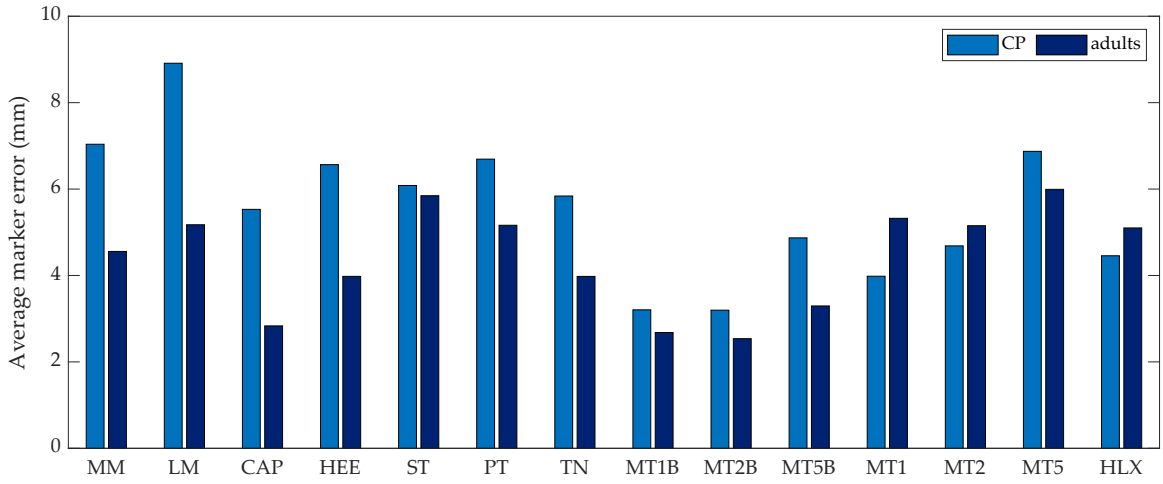


**Figure 3.7:** Average foot marker errors averaged over all subjects and all trials. Foot marker abbreviations are detailed in Table B.1 in Appendix B.

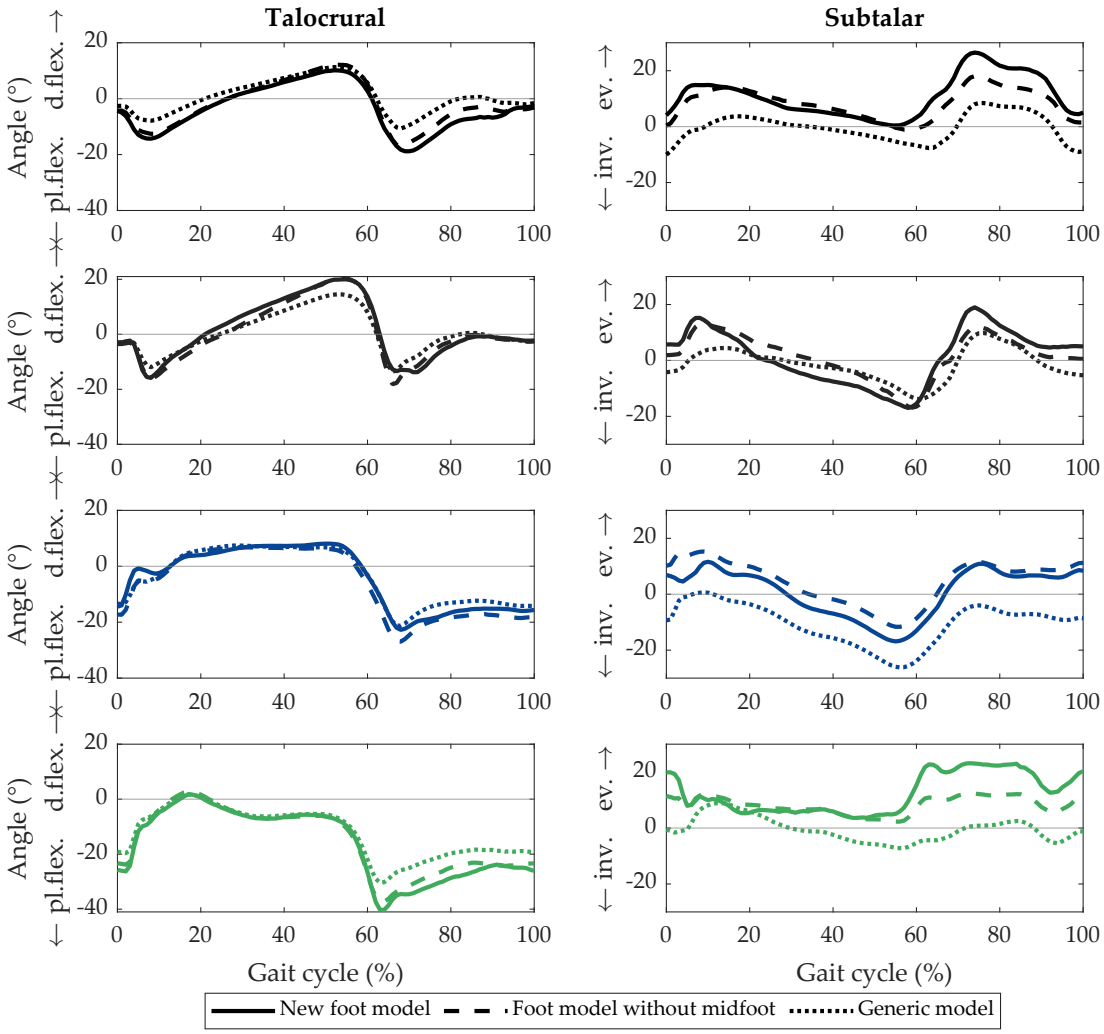


**Figure 3.8:** Comparison of the talocrural and subtalar joint angles resulting from an inverse kinematics analysis with three models: the personalized model, the personalized model without a midfoot (i.e. no Chopart and Lisfranc joints) and the generic model. Results for four representative subjects are shown: the top two rows are control subjects, while the bottom two rows are children with CP (one equinovarus, one cavovarus).

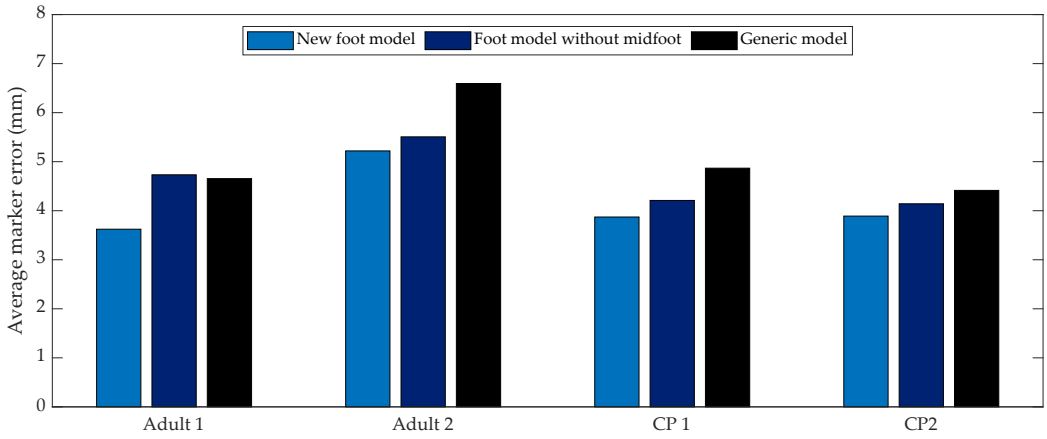


**Figure 3.9:** Foot marker errors averaged over all trials for three models: the personalized model, the personalized model without a midfoot (i.e. no Chopart and Lisfranc joints) and the generic model. Results for four representative subjects are shown: two control subjects and two children with CP (one equinovarus, one cavovarus).

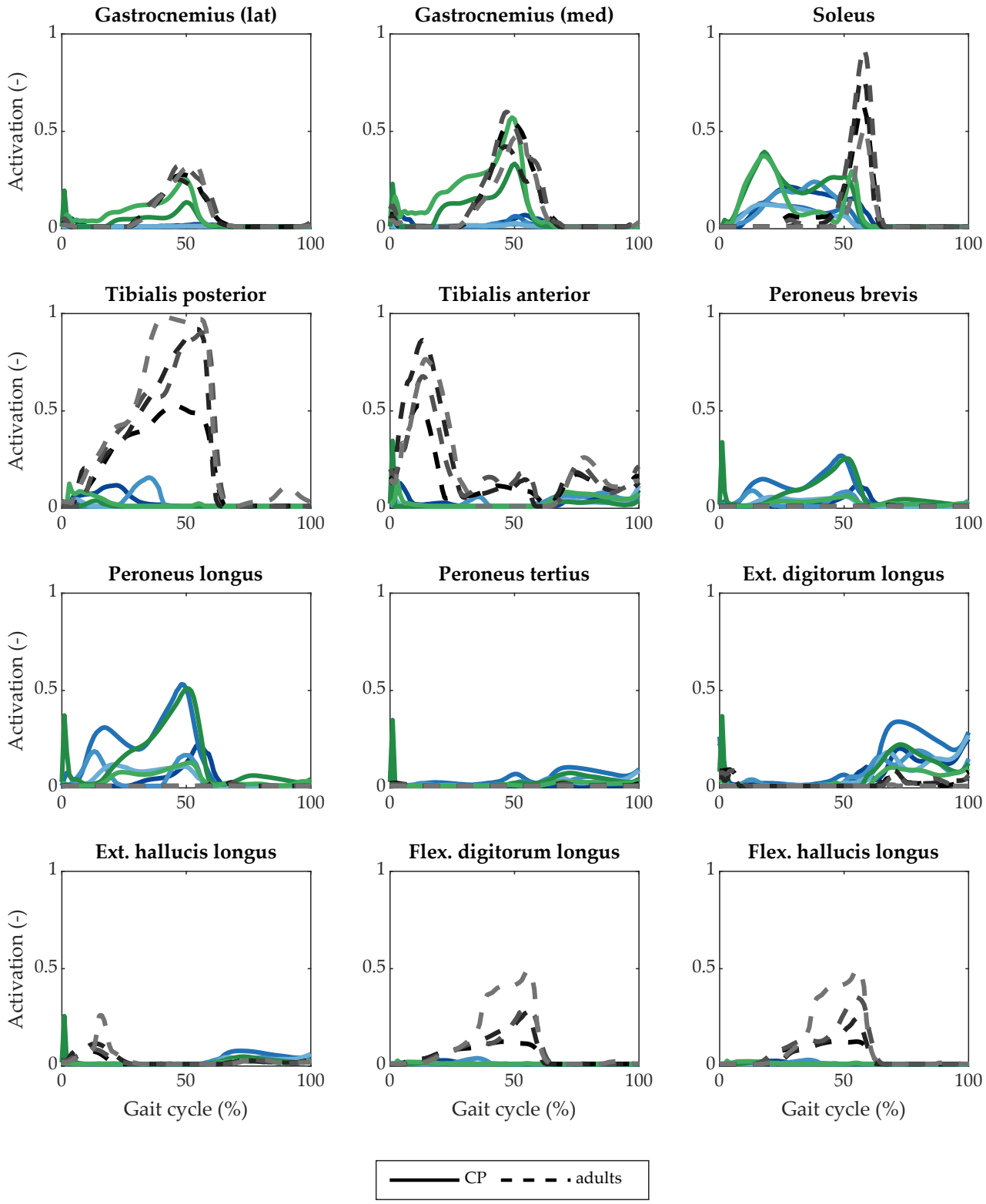


**Figure 3.10:** Static Optimization results: muscle activations of the lower leg muscles. Each line represents one subject. Children with an equinovarus deformity are represented with solid blue lines, while children with a cavovarus deformity are represented with solid green lines.

# 4
# Discussion

The aim of this study was to develop a personalized musculoskeletal foot model, and to apply this model to evaluate how static joint axis orientations and moment arms, and muscle function during gait are altered due to an equinovarus or cavovarus foot deformity in children with CP. This is the first study in which a musculoskeletal foot model was developed based on personalized bone data of feet with bony deformities in weight-bearing conditions.

## 4.1. Joint axis orientations

When comparing the joint axis orientations of the children with CP to the adults with neutral feet, two things stand out. First, there is much more variation in orientation, which can be related to the larger variation in relative bone positions due to the deformity. Second, despite the larger variation, there is frequently an offset in the orientation of the axes.

All joints tend to be more oriented toward vertical in the frontal plane relative to the ground due to the varus deformity, although this difference is only significant in the subtalar and Lisfranc joint. This can be explained by the inverted orientation of the calcaneus relative to the talus, as visualized in Figure 4.1. Due to the relatively similar orientations, this same mechanism applies to the Chopart joint. Functionally, this more vertical orientation of the Chopart joint leads to a more rigid foot and "locking" of the midfoot motion (Aminian & Sangeorzan, 2008; Apostle & Sangeorzan, 2012). Indeed, we observe a smaller average range of motion in the Chopart joint during gait in the CP group (Figure 3.6). This midfoot locking may lead to a reduced stress absorption capability and overloading of the lateral side of the foot (Apostle & Sangeorzan, 2012).

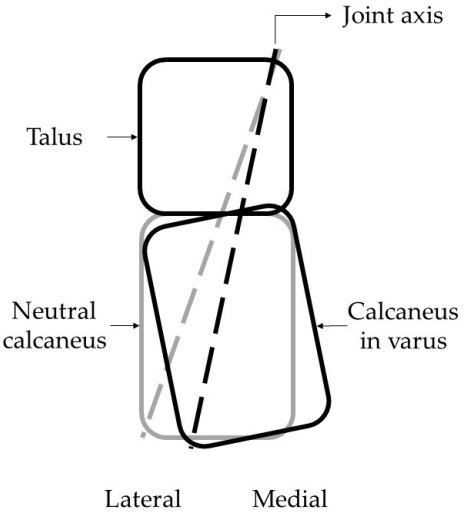


**Figure 4.1:** Frontal view of the talus, calcaneus and subtalar joint, in neutral and varus position.

Figure 4.2 visualizes how the orientation of the Lisfranc axis changes as a function of arch height, with the black figure depicting the supinated (cavovarus) foot. Finally, the rotations in the hindfoot also influence the orientation of the MTP joint, due to a "stacking" effect of the metatarsals, which again leads to overloading of the lateral side of the foot (Apostle & Sangeorzan, 2012).

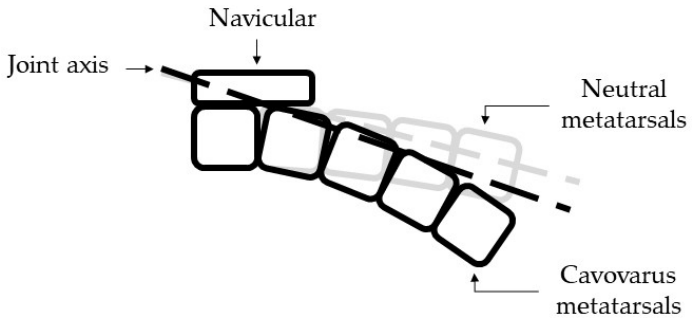


**Figure 4.2:** Frontal view of the first metatarsal axis of the Lisfranc joint, in neutral and cavus position.

## 4.2. Muscle moment arms

Around the talocrural joint, we observe a smaller dorsiflexion moment arm of the tibialis anterior and extensor hallucis longus. The other muscles show no clear difference between the two groups. The tibialis anterior and extensor hallucis longus, together with the extensor digitorum longus and peroneus tertius function as the dorsiflexor muscle group, with the peroneus tertius being a very weak muscle and the tibialis anterior being the most important. With this in mind, with smaller dorsiflexion moment arms the generated dorsiflexion moment at the talocrural joint becomes smaller. We can relate these findings to the kinematics, where we see less dorsiflexion motion in the CP group.

Most subjects with an equinovarus deformity also show larger moment arms in the plantarflexor muscles. This corresponds to larger moment arms of the Achilles tendon that were found in healthy adults in a plantarflexed position (Maganaris et al., 2000; Rugg et al., 1990). On the other hand, the two subjects with cavovarus deformity show smaller plantarflexion moment arms for the triceps surae, which is in correspondence with Deforth et al. (2019).

The inversion-eversion moment arms around the subtalar joint are important to study in relation to the varus deformity. We observe smaller eversion (valgus) moment arms in the extensor digitorum longus and peroneus tertius. The tibialis anterior and extensor hallucis longus even go from an eversion to an inversion moment arm when comparing the control group to the CP group. Interestingly, the tibialis anterior is considered an invertor, and we see an eversion moment arm in the control group in the current study. This discrepancy could be caused by the sensitivity of the line of action of the muscle relative to the subtalar joint axis location. Despite this discrepancy, we can conclude that the varus moment arm of the tibialis anterior is bigger in children with a hindfoot varus deformity. This finding is supported by the work of Lee and Sucato (2008), who found a larger inversion moment arm *in vivo* at an inverted foot posture in healthy adults. The peroneus longus and peroneus brevis are the most important antagonists to the inversion movement. Although the difference is not statistically significant, the eversion moment arm of these muscles is smaller in most subjects, and therefore they would be less effective in counterbalancing the varus deformity.

Spasticity of the tibialis posterior is often seen as an important cause of the varus deformity (Kedem & Scher, 2015). Interestingly, we don't see a change in moment arm around the subtalar joint for this muscle. We can hypothesize that the tibialis posterior is indeed an important cause in the development of the deformity, but that

the deformity is additionally maintained or deteriorated due to the bone positions and altered moment arms of the other muscles.

Finally, around the Chopart joint, the tibialis anterior has significantly larger supination moment arms, but on the other hand both the tibialis posterior and flexor digitorum longus have significantly smaller supination moment arms. The extensor digitorum longus and peroneus tertius do have significantly smaller pronation moment arms to counteract the varus position, but the peroneus tertius is a relatively weak muscle and probably not highly influential in the deformity. The peroneus longus and brevis, who are larger antagonists, show no clear difference in moment arm.

To summarize, we mainly see an important difference in the moment arm of the tibialis anterior around the hindfoot joints: a smaller dorsiflexion moment arm and a larger inversion moment arm. This means the tibialis anterior becomes a less effective dorsiflexor and a more effective invertor with a varus position of the foot. In combination with the larger moment arms of the extensor hallucis longus and smaller moment arms of the antagonist peroneal muscles, this would generate an even larger varus moment in the subtalar joint with the same amount of muscle force, thereby pulling the foot even more towards varus.

## 4.3. Muscle activations

Despite the variable gait patterns in children with CP, we see clear differences in muscle activation between the CP group and the control group. The early activity of the triceps surae in the model in stance can be explained by the forefoot landing that is observed in all children with CP included in this study. We see a decreased activation during push off in the triceps surae, which corresponds to the lower amount of plantarflexion motion observed.

Interestingly, the tibialis posterior and tibialis anterior show decreased activity in the CP group throughout the whole gait cycle. Especially for the tibialis anterior (the primary dorsiflexor), this could be due to the limited dorsiflexion motion during the gait cycle, but both muscles are also the primary invertors of the foot. On the other hand, the peroneal muscles (the primary evertors), show increased activity during the stance phase. This change in activity is probably a stabilization mechanism around the ankle, to resist further inversion during gait. For example, increased peroneal muscle activity was also found in a study where non-affected participants walked on a medially inclined surface, resulting in an inverted foot position (Bavdek et al., 2018). In most subjects, we also observed a decreased moment arm of the peroneal muscles around the subtalar joint, which means the muscle needs to produce more force to generate the same amount of torque around the joint. We could speculate that if the peroneal muscles are not able to generate this increased activity, due to for example weakness, the foot will progress to even more varus due to the weightbearing forces during gait.

To our knowledge, only one study measured electromyography (EMG) activity of the peroneus longus of children with CP with (equino)varus feet (Boulay et al., 2014). They found premature activity of the peroneus longus during swing, and attributed this to a primary neurological impairment, rather than compensatory activity to stabilize the foot. Indeed, we see barely any activation of peroneus longus

and brevis during swing. The much higher activation during stance, however, does suggest a stabilization mechanism. Unfortunately, the amount of activation was not studied by Boulay et al. (2014).

## 4.4. Validation of the model

Ideally, to validate the new foot model, we would compare the results of the model to a "gold standard" measure, such as dual fluoroscopy (for the kinematics) or EMG (for the muscle activations) data of the same participant. Another way is to compare the results of the simulations with reference data from the literature. We will compare the results from the control group only, due to the altered gait pattern of the children with CP.

The presented foot model has a similar pattern, but somewhat larger range of motion in the talocrural joint compared to the AFM (marker model; Schallig et al., 2022), an existing musculoskeletal foot model (Malaquias et al., 2017) and bone pin data (Lundgren et al., 2008). However, all the aforementioned studies describe purely sagittal plane kinematics, while the talocrural joint axis in the current study is oblique and therefore describes motion in all three planes. The pattern of subtalar joint motion we observe is also comparable to the motion of the subtalar joint during gait: eversion in early stance, inversion in late stance and eversion again during the swing phase, although again the range of motion during gait is somewhat larger (Piazza, 2005). Midfoot motion is even more difficult to compare due to the difference in axis definitions. The pattern we observe is similar to the AFM: with less motion in the Lisfranc joint compared to the Chopart joint (Schallig et al., 2022). The average range of motion in the Chopart joint is again a bit larger than seen in the literature, but this could also be explained by the fact that Lundgren et al. (2008) reported motion in the three planes separately, and also measured the motion between calcaneus and cuboid, and talus and navicular separately. The range of motion in the Lisfranc joint is comparable to the motion between the first metatarsal and cuneiform measured with bone pin data. For the MTP joint, both the motion and range is comparable to the published marker data of the AFM (Schallig et al., 2022).

A second measure of the kinematic validity of the model during gait are the marker errors during the inverse kinematic simulations. These were within a few millimeters, which can be considered acceptable errors during these simulations (Hicks et al., 2015). We also compared the current model to the generic *Gait2392* model. Although both models showed relatively low marker errors in the foot, the marker errors in the personalized models were lower in comparison. When comparing the ankle joint angles during gait, more inversion (varus) is measured with the generic model, especially in the CP group. This could be due to the fact that the neutral pose of the personalized model, being based on the WBCT data, already captures part of the inversion, which leads to an offset between the models, or due to a difference in axis position and orientation.

The calculated muscle activations can also be compared to EMG reference data from the literature. The patterns of timing and overall pattern of the muscle activation of the control group match muscle activity measured using surface EMG (Hunt et al., 2001; Zelik et al., 2014) and other studies that utilized Static

Optimization (Falisse et al., 2018; Roelker et al., 2017; Trinler et al., 2019). However, we do observe higher activity than expected in several muscles compared to the EMG patterns, especially the tibialis posterior and first peak of the tibialis anterior. This might again be a result of the subtalar joint being free to move during analysis, without for example ligaments being able to stabilize the joint. Usually, the subtalar joint is locked during this analysis for this reason, along with the other intrinsic foot joints. However, the motion in the subtalar joint is important during gait, especially in this study with varus deformities. As we compared two groups with the subtalar joint unlocked, we would expect this effect to occur in both groups, so the general patterns and amount of activation are still expected to be comparable, but the differences might be exaggerated.

## 4.5. Limitations and future work

The findings of this study have to been seen in light of some limitations, that could be addressed in future work. Firstly, the joint axes in the current model are a representation of what is currently known in the literature, and manually determined based on the selected bony landmarks. Human anatomy is complex however, and this is especially true for the foot. For example, discussion exists about the true degrees of freedom and orientation of the axis in the Chopart and Lisfranc joint complexes. In our model, the joint axes were carefully based on what is currently known about the orientation of the axes relative to the bones. However, morphological fitting of articular surfaces, for example, might improve the accuracy of the joint axes definitions.

In addition, manual selection ("virtual palpation") of the bone locations, as done in this study, may introduce subjectivity and inaccuracies (Hannah et al., 2017; Valente et al., 2014). The bony landmarks were chosen to be as specific as possible, but variation in bone morphology and foot posture occasionally posed challenges when selecting specific landmarks. Selection by multiple researchers and sensitivity tests might improve accuracy and give insight in the sensitivity of the selected landmarks on simulation outcomes. The same is true for the muscle insertions on the foot, which were manually moved to locations on the personalized bone geometry matching the muscle attachments in the *Gait2392* model. Future work could also focus on personalizing muscle paths and insertions based on imaging data of the individual subjects.

Furthermore, the "neutral" position of the foot model was taken as the position of the foot in the WBCT scanner. These scans were captured while the subject stood with the full weight on one leg, which might have influenced the posture and bone positions. In addition, the foot was placed in the model directly below the tibia, which assumes that the tibia was aligned vertically in the scanner. Although the participants were instructed to stand as naturally as possible, looking straight ahead, especially the children with CP sometimes stood with the tibia not vertically oriented, which leads to an offset in the angle of the foot relative to the tibia. However, the part of the tibia included in the scans was not large enough to reliably determine the orientation of the tibia. With a larger scan height, the generic tibia could be registered onto the personalized geometry.

Another thing to note is that only GRF data of the right foot was measured,

so the total GRF during double stance was "incomplete". In OpenSim, this is compensated by residual forces acting on the pelvis. However, simulations without a subtalar joint were comparable to both EMG and Static Optimization results from the literature.

A last limitation concerns the subject groups. The sample sizes in this study were small, so the statistical findings need to be interpreted with caution. Although all participants with CP had a hindfoot varus deformity, the degree of the deformity was variable. In addition, the control group consisted of adults, and not age-matched controls, due to practical and ethical reasons. However, with the age of the children in this study, most feet would be at the end of growth.

There are possibilities for further extension of the model and future applications. In the current model, the ligaments and intrinsic muscles of the foot were not included. Including these could improve, for example, the Static Optimization simulations (which can then include the intrinsic joints of the foot), and it might give more insight in planovalgus foot deformities, as these structures are important for support of the arch of the foot (Angin et al., 2014; Angin et al., 2018). However, there is currently no conclusive evidence about the mechanical behavior of the ligaments and intrinsic muscles of the foot (McKeon et al., 2015; Nie et al., 2017; Soysa et al., 2012). The focus of the current study was to capture the influence of the skeletal morphology on muscle function in isolation, but the model can be extended to also include personalized muscle architecture, to get further insight in the development of the deformity. Not only muscle paths and insertions could be implemented, but also altered musculotendon parameters (Veerkamp et al., 2022), isometric muscle force (Kainz et al., 2018), or neuromuscular control (Veerkamp et al., 2019). Future applications of these type of models could also be simulation of interventions, such as bony surgery or tendon transfers.

# 5
# Conclusion

In this study, we developed a personalized musculoskeletal foot model based on weight-bearing CT data, to evaluate how muscle function is altered due to a hindfoot varus deformity in children with cerebral palsy. We found that the structural differences that occur in the foot due to the varus deformity lead to differences in muscle function, that could lead to a progression of the deformity once the deformity is present. The joint axis orientations were altered in the CP group, with more variation between subjects in this group. In most subjects, changes in axis orientations were observed that may lead to a more rigid foot. Furthermore, the altered moment arms of the muscles generally led to a more effective varus moment around the hindfoot, which may contribute to further progression of the deformity. During gait, the activity of the invertor muscles was decreased during stance, while the activity of the evertor muscles increased, which may be a mechanism to stabilize the foot and resist further varus. These findings contribute to a better understanding of the altered muscle function due to foot deformities. Hopefully, with these models, we can eventually contribute to the improvement of treatment to prevent progression of foot deformities in children with cerebral palsy.

# References


Aisen, M. L., Kerkovich, D., Mast, J., Mulroy, S., Wren, T. A., Kay, R. M., & Rethlefsen, S. A. (2011). Cerebral palsy: Clinical care and neurological rehabilitation. *The Lancet Neurology*, *10*(9), 844–852. https://doi.org/10.1016/S1474-4422(11)70176-4

Aminian, A., & Sangeorzan, B. J. (2008). The anatomy of cavus foot deformity. *Foot and Ankle Clinics*, *13*(2), 191–198. https://doi.org/10.1016/j.fcl.2008.01.004

Anderson, F. C., & Pandy, M. G. (1999). A dynamic optimization solution for vertical jumping in three dimensions. *Computer Methods in Biomechanics and Biomedical Engineering*, *2*(3), 201–231. https://doi.org/10.1080/10255849908907988

Anderson, F. C., & Pandy, M. G. (2001). Dynamic optimization of human walking. *Journal of Biomechanical Engineering*, *123*(5), 381–390. https://doi.org/10.1115/1.1392310

Angin, S., Crofts, G., Mickle, K. J., & Nester, C. J. (2014). Ultrasound evaluation of foot muscles and plantar fascia in pes planus. *Gait & Posture*, *40*(1), 48–52. https://doi.org/10.1016/j.gaitpost.2014.02.008

Angin, S., Mickle, K. J., & Nester, C. J. (2018). Contributions of foot muscles and plantar fascia morphology to foot posture. *Gait & Posture*, *61*, 238–242. https://doi.org/10.1016/j.gaitpost.2018.01.022

Apostle, K. L., & Sangeorzan, B. J. (2012). Anatomy of the varus foot and ankle. *Foot and Ankle Clinics*, *17*(1), 1–11. https://doi.org/10.1016/j.fcl.2011.11.001

Arnold, A. S., & Delp, S. L. (2005). Computer modeling of gait abnormalities in cerebral palsy: Application to treatment planning. *Theoretical Issues in Ergonomics Science*, *6*(3-4), 305–312. https://doi.org/10.1080/14639220412331329636

Bavdek, R., Zdolšek, A., Strojnik, V., & Dolenec, A. (2018). Peroneal muscle activity during different types of walking. *Journal of Foot and Ankle Research*, *11*, 50. https://doi.org/10.1186/s13047-018-0291-0

Blemker, S. S., Asakawa, D. S., Gold, G. E., & Delp, S. L. (2007). Image-based musculoskeletal modeling: Applications, advances, and future opportunities. *Journal of Magnetic Resonance Imaging*, *25*(2), 441–451. https://doi.org/10.1002/jmri.20805

Bloom, T., & Sabharwal, S. (2022). Surgical management of foot and ankle deformities in cerebral palsy. *Clinics in Podiatric Medicine and Surgery*, *39*(1), 37–55. https://doi.org/10.1016/j.cpm.2021.09.001

Bosmans, L., Wesseling, M., Desloovere, K., Molenaers, G., Scheys, L., & Jonkers, I. (2014). Hip contact force in presence of aberrant bone geometry during normal and pathological gait. *Journal of Orthopaedic Research*, *32*(11), 1406–1415. https://doi.org/10.1002/jor.22698

Boulay, C., Jacquemier, M., Pomero, V., Castanier, E., Authier, G., Chabrol, B., Bollini, G., Jouve, J.-L., & Viehweger, E. (2014). Dynamic EMG of peroneus longus in hemiplegic children with equinovarus. *Annals of Physical and Rehabilitation Medicine*, *57*(3), 185–192. https://doi.org/10.1016/j.rehab.2014.02.004

Broos, M., Berardo, S., Dobbe, J., Maas, M., Streekstra, G., & Wellenberg, R. (2021). Geometric 3D analyses of the foot and ankle using weight-bearing and non weight-bearing cone-beam CT images: The new standard? *European journal of radiology*, *138*, 109674. https://doi.org/10.1016/j.ejrad.2021.109674

Cappozzo, A., Catani, F., Croce, U. D., & Leardini, A. (1995). Position and orientation in space of bones during movement: Anatomical frame definition and determination. *Clinical Biomechanics*, *10*(4), 171–178. https://doi.org/10.1016/0268-0033(95)91394-t

Carnahan, K. D., Arner, M., & Hägglund, G. (2007). Association between gross motor function (GMFCS) and manual ability (MACS) in children with cerebral palsy. A population-based study of 359 children. *BMC Musculoskeletal Disorders*, *8*(1), 1–7. https://doi.org/10.1186/1471-2474-8-50

Correa, T. A., Baker, R., Kerr Graham, H., & Pandy, M. G. (2011). Accuracy of generic musculoskeletal models in predicting the functional roles of muscles in human gait. *Journal of Biomechanics*, *44*(11), 2096–2105. https://doi.org/10.1016/j.jbiomech.2011.05.023

Davids, J. R. (2010). The foot and ankle in cerebral palsy. *Orthopedic Clinics of North America*, *41*(4), 579–593. https://doi.org/10.1016/j.ocl.2010.06.002

Day, E. M., & Hahn, M. E. (2019). A comparison of metatarsophalangeal joint center locations on estimated joint moments during running. *Journal of Biomechanics*, *86*, 64–70. https://doi.org/10.1016/j.jbiomech.2019.01.044

De Cesar Netto, C., Schon, L., Thawait, G., Fonseca, L., Chinanuvathana, A., Zbijewski, W., Siewerdsen, J., & Demehri, S. (2017). Flexible adult acquired flatfoot deformity: Comparison between weight-bearing and non-weight-bearing measurements using cone-beam computed tomography. *The Journal of Bone and Joint Surgery*, *99*(18), e98. https://doi.org/10.2106/JBJS.16.01366

Deforth, M., Zwicky, L., Horn, T., & Hintermann, B. (2019). The effect of foot type on the Achilles tendon moment arm and biomechanics. *The Foot*, *38*, 91–94. https://doi.org/10.1016/j.foot.2018.10.003

Delp, S. L., Anderson, F. C., Arnold, A. S., Loan, P., Habib, A., John, C. T., Guendelman, E., & Thelen, D. G. (2007). OpenSim: Open-source software to create and analyze dynamic simulations of movement. *IEEE Transactions on Biomedical Engineering*, *54*(11), 1940–1950. https://doi.org/10.1109/TBME.2007.901024

Delp, S. L., Loan, J. P., Hoy, M. G., Zajac, F. E., Topp, E. L., & Rosen, J. M. (1990). An interactive graphics-based model of the lower extremity to study orthopaedic surgical procedures. *IEEE Transactions on Biomedical Engineering*, *37*(8), 757–767. https://doi.org/10.1109/10.102791

Dempster, W. T. (1955). *Space requirements of the seated operator: Geometrical, kinematic, and mechanical aspects of the body with special reference to the limbs* (tech. rep.). University of Michigan.

Deschamps, K., Eerdekens, M., Desmet, D., Matricali, G. A., Wuite, S., & Staes, F. (2017). Estimation of foot joint kinetics in three and four segment foot models using an existing proportionality scheme: Application in paediatric barefoot walking. *Journal of Biomechanics*, *61*, 168–175. https://doi.org/10.1016/j.clinbiomech.2019.05.005

Eerdekens, M., Staes, F., Matricali, G. A., Wuite, S., Peerlinck, K., & Deschamps, K. (2019). Quantifying clinical misinterpretations associated to one-segment

kinetic foot modelling in both a healthy and patient population. *Clinical Biomechanics*, *67*, 160–165. https://doi.org/10.1016/j.clinbiomech.2019.05.005

Falisse, A., Rossom, S. V., Gijsbers, J., Steenbrink, F., Basten, B. J. van, Jonkers, I., Bogert, A. J. van den, & Groote, F. D. (2018). OpenSim versus Human Body Model: A comparison study for the lower limbs during gait. *Journal of Applied Biomechanics*, *34*(6), 496–502. https://doi.org/10.1123/jab.2017-0156

Flux, E., Van der Krogt, M., Cappa, P., Petrarca, M., Desloovere, K., & Harlaar, J. (2020). The Human Body Model versus conventional gait models for kinematic gait analysis in children with cerebral palsy. *Human Movement Science*, *70*, 102585. https://doi.org/10.1016/j.humov.2020.102585

Gormley, M. E. (2001). Treatment of neuromuscular and musculoskeletal problems in cerebral palsy. *Pediatric Rehabilitation*, *4*(1), 5–16. https://doi.org/10.1080/13638490151068393

Hannah, I., Montefiori, E., Modenese, L., Prinold, J., Viceconti, M., & Mazza, C. (2017). Sensitivity of a juvenile subject-specific musculoskeletal model of the ankle joint to the variability of operator-dependent input. *Proceedings of the Institution of Mechanical Engineers, Part H: Journal of Engineering in Medicine*, *231*(5), 415–422. https://doi.org/10.1177/0954411917701167

Hicks, J. L., Uchida, T. K., Seth, A., Rajagopal, A., & Delp, S. L. (2015). Is my model good enough? Best practices for verification and validation of musculoskeletal models and simulations of movement. *Journal of Biomechanical Engineering*, *137*(2). https://doi.org/10.1115/1.4029304

Hicks, J. (1953). The mechanics of the foot: I. The joints. *Journal of Anatomy*, *87*(4), 345.

Hirschmann, A., Pfirrmann, C. W., Klammer, G., Espinosa, N., & Buck, F. M. (2014). Upright cone CT of the hindfoot: Comparison of the non-weight-bearing with the upright weight-bearing position. *European Radiology*, *24*(3), 553–558. https://doi.org/10.1007/s00330-013-3028-2

Hunt, A. E., Smith, R. M., & Torode, M. (2001). Extrinsic muscle activity, foot motion and ankle joint moments during the stance phase of walking. *Foot & Ankle International*, *22*(1), 31–41. https://doi.org/10.1177/107110070102200105

Isman, R., & Inman, V. (1969). Anthropometric studies of the human foot and ankle. *Bulletin of Prosthetics Research*, 97–129.

Jakob, R., Haertel, M., & Stussi, E. (1980). Tibial torsion calculated by computerised tomography and compared to other methods of measurement. *The Journal of Bone and Joint Surgery. British volume*, *62*(2), 238–242. https://doi.org/10.1302/0301-620X.62B2.7364840

Kainz, H., Goudriaan, M., Falisse, A., Huenaerts, C., Desloovere, K., De Groote, F., & Jonkers, I. (2018). The influence of maximum isometric muscle force scaling on estimated muscle forces from musculoskeletal models of children with cerebral palsy. *Gait & posture*, *65*, 213–220. https://doi.org/10.1016/j.gaitpost.2018.07.172

Kainz, H., Wesseling, M., & Jonkers, I. (2021). Generic scaled versus subject-specific models for the calculation of musculoskeletal loading in cerebral palsy gait: Effect of personalized musculoskeletal geometry outweighs the effect of personalized neural control. *Clinical Biomechanics*, *87*, 105402. https://doi.org/10.1016/j.clinbiomech.2021.105402

Kedem, P., & Scher, D. M. (2015). Foot deformities in children with cerebral palsy. *Current Opinion in Pediatrics*, *27*(1), 67–74. https://doi.org/10.1097/mop.0000000000000180

Kewley, A. (2023). *OpenSim Creator*. https://doi.org/10.5281/zenodo.7575937

Kirby, K. A. (2001). Subtalar joint axis location and rotational equilibrium theory of foot function. *Journal of the American Podiatric Medical Association*, *91*(9), 465–487. https://doi.org/10.7547/87507315-91-9-465

Leardini, A., Benedetti, M. G., Berti, L., Bettinelli, D., Nativo, R., & Giannini, S. (2007). Rear-foot, mid-foot and fore-foot motion during the stance phase of gait. *Gait & Posture*, *25*(3), 453–462. https://doi.org/10.1016/j.gaitpost.2006.05.017

Leardini, A., Durante, S., Belvedere, C., Caravaggi, P., Carrara, C., Berti, L., Lullini, G., Giacomozzi, C., Durastanti, G., Ortolani, M., et al. (2019). Weight-bearing CT technology in musculoskeletal pathologies of the lower limbs: Techniques, initial applications, and preliminary combinations with gait-analysis measurements at the Istituto Ortopedico Rizzoli. *Seminars in Musculoskeletal Radiology*, *23*(6), 643–656. https://doi.org/10.1055/s-0039-1697939

Ledoux, W. R., Rohr, E. S., Ching, R. P., & Sangeorzan, B. J. (2006). Effect of foot shape on the three-dimensional position of foot bones. *Journal of Orthopaedic Research*, *24*(12), 2176–2186. https://doi.org/10.1002/jor.20262

Lee, M. C., & Sucato, D. J. (2008). Pediatric issues with cavovarus foot deformities. *Foot and Ankle Clinics*, *13*(2), 199–219. https://doi.org/10.1016/j.fcl.2008.01.002

Lundberg, A., & Svensson, O. (1993). The axes of rotation of the talocalcaneal and talonavicular joints. *The Foot*, *3*(2), 65–70. https://doi.org/10.1016/0958-2592(93)90064-A

Lundberg, A., Svensson, O., Nemeth, G., & Selvik, G. (1989). The axis of rotation of the ankle joint. *The Journal of Bone and Joint Surgery. British volume*, *71*(1), 94–99. https://doi.org/10.1302/0301-620X.71B1.2915016

Lundgren, P., Nester, C., Liu, A., Arndt, A., Jones, R., Stacoff, A., Wolf, P., & Lundberg, A. (2008). Invasive in vivo measurement of rear-, mid-and forefoot motion during walking. *Gait & Posture*, *28*(1), 93–100. https://doi.org/10.1016/j.gaitpost.2007.10.009

Maganaris, C. N., Baltzopoulos, V., & Sargeant, A. J. (2000). In vivo measurement-based estimations of the human Achilles tendon moment arm. *European Journal of Applied Physiology*, *83*, 363–369. https://doi.org/10.1007/s004210000247

Maharaj, J. N., Rainbow, M. J., Cresswell, A. G., Kessler, S., Konow, N., Gehring, D., & Lichtwark, G. A. (2021). Modelling the complexity of the foot and ankle during human locomotion: The development and validation of a multi-segment foot model using biplanar videoradiography. *Computer Methods in Biomechanics and Biomedical Engineering*, *25*(5), 554–565. https://doi.org/10.1080/10255842.2021.1968844

Malaquias, T. M., Silveira, C., Aerts, W., De Groote, F., Dereymaeker, G., Vander Sloten, J., & Jonkers, I. (2017). Extended foot-ankle musculoskeletal models for application in movement analysis. *Computer Methods in Biomechanics and Biomedical Engineering*, *20*(2), 153–159. https://doi.org/10.1080/10255842.2016.1206533

McKeon, P. O., Hertel, J., Bramble, D., & Davis, I. (2015). The foot core system: A new paradigm for understanding intrinsic foot muscle function. *British Journal*

*of Sports Medicine*, *49*(5), 290–290. https://doi.org/10.1136/bjsports-2013-092690

Miller, F. (2020). Foot deformities impact on cerebral palsy gait. In *Cerebral palsy* (pp. 1517–1532). Springer. https://doi.org/10.1007/978-3-319-74558-9_201

Miller, F., & Church, C. (2020). Natural history of foot deformities in children with cerebral palsy. In *Cerebral palsy* (pp. 2223–2232). Springer. https://doi.org/10.1007/978-3-319-74558-9_142

Nester, C. J. (1997). Rearfoot complex: A review of its interdependent components, axis orientation and functional model. *The Foot*, *7*(2), 86–96. https://doi.org/10.1016/S0958-2592(97)90054-7

Nester, C. J. (1998). Review of literature on the axis of rotation at the sub talar joint. *The Foot*, *8*(3), 111–118. https://doi.org/10.1016/S0958-2592(98)90042-6

Nester, C. J., Findlow, A., & Bowker, P. (2001). Scientific approach to the axis of rotation at the midtarsal joint. *Journal of the American Podiatric Medical Association*, *91*(2), 68–73. https://doi.org/10.7547/87507315-91-2-68

Nie, B., Panzer, M. B., Mane, A., Mait, A. R., Donlon, J.-P., Forman, J. L., & Kent, R. W. (2017). Determination of the in situ mechanical behavior of ankle ligaments. *Journal of the Mechanical Behavior of Biomedical Materials*, *65*, 502–512. https://doi.org/10.1016/j.jmbbm.2016.09.010

Nozaki, S., Watanabe, K., & Katayose, M. (2017). Three-dimensional morphometric analysis of the talus: Implication for variations in kinematics of the subtalar joint. *Surgical and Radiologic Anatomy*, *39*(10), 1097–1106. https://doi.org/10.1007/s00276-017-1851-x

O'Connell, P. A., D'Souza, L., Dudeney, S., & Stephens, M. (1998). Foot deformities in children with cerebral palsy. *Journal of Pediatric Orthopaedics*, *18*(6), 743–747. https://doi.org/10.1097/00004694-199811000-00009

Peña Fernández, M., Hoxha, D., Chan, O., Mordecai, S., Blunn, G. W., Tozzi, G., & Goldberg, A. (2020). Centre of rotation of the human subtalar joint using weight-bearing clinical computed tomography. *Scientific Reports*, *10*(1), 1–14. https://doi.org/10.1038/s41598-020-57912-z

Piazza, S. J. (2005). Mechanics of the subtalar joint and its function during walking. *Foot and Ankle Clinics*, *10*(3), 425–442. https://doi.org/10.1016/j.fcl.2005.04.001

Pietak, A., Ma, S., Beck, C. W., & Stringer, M. D. (2013). Fundamental ratios and logarithmic periodicity in human limb bones. *Journal of Anatomy*, *222*(5), 526–537. https://doi.org/10.1111/joa.12041

Pothrat, C., Authier, G., Viehweger, E., Berton, E., & Rao, G. (2015). One-and multi-segment foot models lead to opposite results on ankle joint kinematics during gait: Implications for clinical assessment. *Clinical Biomechanics*, *30*(5), 493–499. https://doi.org/10.1016/j.clinbiomech.2015.03.004

Prinold, J., Mazzà, C., Marco, R. D., Hannah, I. G., Malattia, C., Magni-Manzoni, S., Petrarca, M., Ronchetti, A., Horatio, L. T. de, Dijkhuizen, E. H. P. van, Wesarg, S., & Viceconti, M. (2016). A patient-specific foot model for the estimate of ankle joint forces in patients with Juvenile Idiopathic Arthritis. *Annals of Biomedical Engineering*, *44*(1), 247–257. https://doi.org/10.1007/s10439-015-1451-z

Raychoudhury, S., Hu, D., & Ren, L. (2014). Three-dimensional kinematics of the human metatarsophalangeal joint during level walking. *Frontiers in Bioengineering and Biotechnology*, *2*, 73. https://doi.org/10.3389/fbioe.2014.00073

Redmond, A. C., Crane, Y. Z., & Menz, H. B. (2008). Normative values for the Foot Posture Index. *Journal of Foot and Ankle research*, *1*, 6. https://doi.org/10.1186/1757-1146-1-6

Reinbolt, J. A., Seth, A., & Delp, S. L. (2011). Simulation of human movement: Applications using OpenSim. *Procedia Iutam*, *2*, 186–198. https://doi.org/10.1016/j.piutam.2011.04.019

Roelker, S. A., Caruthers, E. J., Baker, R. K., Pelz, N. C., Chaudhari, A. M. W., & Siston, R. A. (2017). Interpreting musculoskeletal models and dynamic simulations: Causes and effects of differences between models [Supplementary material]. *Annals of Biomedical Engineering*, *45*(11), 2635–2647. https://doi.org/10.1007/s10439-017-1894-5

Rugg, S., Gregor, R., Mandelbaum, B., & Chiu, L. (1990). In vivo moment arm calculations at the ankle using magnetic resonance imaging (MRI). *Journal of Biomechanics*, *23*(5), 495–501. https://doi.org/10.1016/0021-9290(90)90305-m

Sadowska, M., Sarecka-Hujar, B., & Kopyta, I. (2020). Cerebral palsy: Current opinions on definition, epidemiology, risk factors, classification and treatment options. *Neuropsychiatric Disease and Treatment*, *16*, 1505–1518. https://doi.org/10.2147/NDT.S235165

Saraswat, P., Andersen, M. S., & MacWilliams, B. A. (2010). A musculoskeletal foot model for clinical gait analysis. *Journal of Biomechanics*, *43*(9), 1645–1652. https://doi.org/10.1016/j.jbiomech.2010.03.005

Schallig, W., Noort, J. C. van den, Piening, M., Streekstra, G. J., Maas, M., Krogt, M. M. van der, & Harlaar, J. (2022). The Amsterdam Foot Model: A clinically informed multi-segment foot model developed to minimize measurement errors in foot kinematics. *Journal of Foot and Ankle Research*, *15*, 46. https://doi.org/10.1186/s13047-022-00543-6

Schünke, M., Schulte, E., Schumacher, U., Voll, M., & Wesker, K. (2016). *Prometheus anatomische atlas: Algemene anatomie en bewegingsapparaat* (Fourth edition). Bohn Stafleu van Loghum.

Seth, A., Hicks, J. L., Uchida, T. K., Habib, A., Dembia, C. L., Dunne, J. J., Ong, C. F., DeMers, M. S., Rajagopal, A., Millard, M., et al. (2018). OpenSim: Simulating musculoskeletal dynamics and neuromuscular control to study human and animal movement. *PLoS Computational Biology*, *14*(7), e1006223. https://doi.org/10.1371/journal.pcbi.1006223

Sherman, M. A., Seth, A., & Delp, S. L. (2013). What is a moment arm? Calculating muscle effectiveness in biomechanical models using generalized coordinates. *International Design Engineering Technical Conferences and Computers and Information in Engineering Conference*, *55973*, V07BT10A052. https://doi.org/10.1115/DETC2013-13633

Sikidar, A., & Kalyanasundaram, D. (2022). An open-source OpenSim® ankle-foot musculoskeletal model for assessment of strains and forces in dense connective tissues. *Computer Methods and Programs in Biomedicine*, *224*, 106994. https://doi.org/10.1016/j.cmpb.2022.106994

Soysa, A., Hiller, C., Refshauge, K., & Burns, J. (2012). Importance and challenges of measuring intrinsic foot muscle strength. *Journal of Foot and Ankle Research*, *5*(1), 1–14. https://doi.org/10.1186/1757-1146-5-29

Theologis, T. (2013). Lever arm dysfunction in cerebral palsy gait. *Journal of Children's Orthopaedics*, *7*(5), 379–382. https://doi.org/10.1007/s11832-013-0510-y

Trinler, U., Schwameder, H., Baker, R., & Alexander, N. (2019). Muscle force estimation in clinical gait analysis using AnyBody and OpenSim. *Journal of Biomechanics*, *86*, 55–63. https://doi.org/10.1016/j.jbiomech.2019.01.045

Tweed, J. L., Campbell, J., Thompson, R., & Curran, M. (2008). The function of the midtarsal joint: A review of the literature. *The Foot*, *18*(2), 106–112. https://doi.org/10.1016/j.foot.2008.01.002

Valente, G., Pitto, L., Testi, D., Seth, A., Delp, S. L., Stagni, R., Viceconti, M., & Taddei, F. (2014). Are subject-specific musculoskeletal models robust to the uncertainties in parameter identification? *PloS one*, *9*(11), e112625. https://doi.org/10.1371/journal.pone.0112625

Van den Bogert, A. J., Geijtenbeek, T., Even-Zohar, O., Steenbrink, F., & Hardin, E. C. (2013). A real-time system for biomechanical analysis of human movement and muscle function. *Medical & Biological Engineering & Computing*, *51*(10), 1069–1077. https://doi.org/10.1007/s11517-013-1076-z

Veerkamp, K., Kainz, H., Killen, B. A., Jónasdóttir, H., & Krogt, M. M. van der. (2021). Torsion Tool: An automated tool for personalising femoral and tibial geometries in OpenSim musculoskeletal models. *Journal of Biomechanics*, *125*, 110589. https://doi.org/10.1016/j.jbiomech.2021.110589

Veerkamp, K., Krogt, M. M. van der, Harlaar, J., O'Brien, T. D., Kalkman, B., Seth, A., & Bar-On, L. (2022). Personalisation of plantarflexor musculotendon model parameters in children with cerebral palsy. *Annals of Biomedical Engineering*, 1–13. https://doi.org/10.1007/s10439-022-03107-8

Veerkamp, K., Schallig, W., Harlaar, J., Pizzolato, C., Carty, C. P., Lloyd, D. G., & Krogt, M. M. van der. (2019). The effects of electromyography-assisted modelling in estimating musculotendon forces during gait in children with cerebral palsy. *Journal of Biomechanics*, *92*, 45–53.

Wellenberg, R., Schallig, W., Steenbergen, P., Tex, P. d., Dobbe, J., Streekstra, G., Witbreuk, M., Buizer, A., & Maas, M. (2022). Assessment of foot deformities in individuals with cerebral palsy using weight-bearing CT. *Skeletal Radiology*, 1–8. https://doi.org/10.1007/s00256-022-04272-6

Wesseling, M., Bosmans, L., Dijck, C. V., Sloten, J. V., Wirix-Speetjens, R., & Jonkers, I. (2019). Non-rigid deformation to include subject-specific detail in musculoskeletal models of CP children with proximal femoral deformity and its effect on muscle and contact forces during gait. *Computer Methods in Biomechanics and Biomedical Engineering*, *22*(4), 376–385. https://doi.org/10.1080/10255842.2018.1558216

Yamaguchi, G. T., & Zajac, F. E. (1989). A planar model of the knee joint to characterize the knee extensor mechanism. *Journal of Biomechanics*, *22*(1), 1–10. https://doi.org/10.1016/0021-9290(89)90179-6

Zandbergen, M. A., Schallig, W., Stebbins, J. A., Harlaar, J., & Krogt, M. M. van der. (2020). The effect of mono- versus multi-segment musculoskeletal models of

the foot on simulated triceps surae lengths in pathological and healthy gait. *Gait & Posture*, *77*, 14–19. https://doi.org/10.1016/j.gaitpost.2020.01.010

Zelik, K. E., Scaleia, V. L., Ivanenko, Y. P., & Lacquaniti, F. (2014). Coordination of intrinsic and extrinsic foot muscles during walking. *European Journal of Applied Physiology*, *115*(4), 691–701. https://doi.org/10.1007/s00421-014-3056-x

Zeni, J. A., Richards, J. G., & Higginson, J. S. (2008). Two simple methods for determining gait events during treadmill and overground walking using kinematic data. *Gait & Posture*, *27*(4), 710–714. https://doi.org/10.1016/j.gaitpost.2007.07.007

# A
# Inertia tensor calculations

To calculate the inertia tensor for each segment, the dimensions of each segment were required. These dimensions were calculated based on the distances between selected marker pairs.

The height of the talus was calculated using the midpoint between the markers on the malleoli (MM and LM), and the midpoint between the navicular (TN) and (virtual) cuboid (CUB) markers. The average distance between these two points was seen as the height of the talus. The width of the talus was calculated as the distance between the markers on the sustentaculum tali (ST) and peroneal tubercle (PT), with a correction for the marker diameter. The height of the talus was calculated as the average distance between the LM and PT markers, and between the MM and ST markers.

The length of the calcaneus was calculated using the midpoint between the TN and (virtual) CUB markers, and the marker on the heel (HEE). The radius of the calcaneus was calculated as half the distance between the ST and PT markers, with a correction for the marker diameter.

The length of the midfoot was calculated using the midpoint between the TN and (virtual) CUB markers, and the midpoint between the virtual MT12B and MT25B markers. In turn, the MT12B marker is the midpoint between the markers on the base of the first and second metatarsal (MT1B and MT2B), and the MT25B marker is the midpoint between the markers on the base of the second and the fifth metatarsal (MT2B and MT5B) (see also Appendix C). The major radius (in the z-direction) was calculated as half the distance between the TN and CUB markers, with a correction for the marker diameter. The minor radius (in the y-direction) was calculated as half the distance between the MT2B marker and the ground, with a correction for the marker diameter.

The length of the forefoot was calculated using the midpoint between the virtual MT12B and MT25B markers, and the midpoint between the virtual MT12 and MT25 markers, with MT12 being the midpoint between the markers on the first and second metatarsal heads (MT1 and MT2), and MT25 the midpoint between the markers on the second and fifth metatarsal heads (MT2 and MT5). The major radius (in the z-direction) was calculated as half the distance between the MT1 and MT5 markers. The minor radius (in the y-direction) was calculated as half the average height of the MT2 and MT2B markers relative to the ground.

The length of the toes was calculated as 1/1.4 of the length of the forefoot. This was based on the average ratio between metatarsal and phalanges length in Pietak et al. (2013). The major radius (in the z-direction) was equal to the forefoot. The minor radius (in the y-direction) was calculated as half the average height of the marker on the hallux (HLX), with a correction for the marker diameter.

The moments of inertia of the talus were subsequently calculated as (Vallery & Schwab, 2020):

$$I_{xx,cuboid} = \frac{1}{12} \cdot m \cdot (h^2 + w^2); \tag{A.1}$$

$$I_{yy,cuboid} = \frac{1}{12} \cdot m \cdot (l^2 + w^2); \tag{A.2}$$

$$I_{zz,cuboid} = \frac{1}{12} \cdot m \cdot (l^2 + h^2); \tag{A.3}$$

with $m$ the mass; $l$ the length of the segment (dimension in x-direction); $h$ the height of the segment (dimension in y-direction); and $w$ the width of the segment (dimension in z-direction).

The moments of inertia of the calcaneus were calculated as (Vallery & Schwab, 2020):

$$I_{xx,cylinder} = \frac{1}{2} \cdot m \cdot r^2; \tag{A.4}$$

$$I_{yy,cylinder} = I_{zz,cylinder} = \frac{1}{12} \cdot m \cdot (3 \cdot r^2 + l^2); \tag{A.5}$$

with $r$ the radius of the segment.

Finally, the moments of inertia of the midfoot, forefoot and toes were calculated as (Bruening, 2009):

$$I_{xx,ell.cylinder} = \frac{1}{4} \cdot m \cdot (r_y^2 + r_z^2); \tag{A.6}$$

$$I_{yy,ell.cylinder} = \frac{1}{12} \cdot m \cdot (3 \cdot r_z^2 + l^2); \tag{A.7}$$

$$I_{zz,ell.cylinder} = \frac{1}{12} \cdot m \cdot (3 \cdot r_y^2 + l^2); \tag{A.8}$$

with $r_y$ the radius in y-direction and $r_z$ the radius in z-direction.

# References

Bruening, D. A. (2009). *A kinetic multi-segment foot model with preliminary applications in clinical gait analysis* (Doctoral dissertation). University of Delaware.

Pietak, A., Ma, S., Beck, C. W., & Stringer, M. D. (2013). Fundamental ratios and logarithmic periodicity in human limb bones. *Journal of Anatomy*, *222*(5), 526–537. https://doi.org/10.1111/joa.12041

Vallery, H., & Schwab, A. L. (2020). *Advanced dynamics* (Third edition). Stichting Newton-Euler.

# B

# Amsterdam Foot Model marker set

This appendix lists the locations of the markers on the foot, used during the gait analyses.

**Table B.1:** Marker set of the Amsterdam Foot Model (Schallig et al., 2022).

| Segment | Abbreviation | Specific location |
|---|---|---|
| Shank | TT: tibial tuberosity | Most anterior prominence of the tibial tuberosity |
| | FH: fibular head | Most proximal apex of the fibular head |
| | ASHA: anterior shin | Halfway the shank in the center of the tibia |
| | LSHA: lateral shin | On the line between FH and LM at the height of ASHA |
| | LM: lateral malleolus | Distal apex of the lateral malleolus |
| | MM: medial malleolus | Distal apex of the medial malleolus |
| Hindfoot | CAP: proximally on posterior aspect of calcaneus | Proximally on the midline of the calcaneus posterior aspect (i.e. Achilles tendon attachment) |
| | HEE: distally on posterior aspect of calcaneus | Distally on the midline of the calcaneus posterior aspect |
| | ST: sustentaculum tali | Most medial apex of the sustentaculum tali |
| | PT: peroneal tuberculum | Most lateral apex of the peroneal tubercle |
| Midfoot | TN: navicular tuberosity | Most medial apex of the navicular tuberosity |
| Forefoot | MT1B: base metatarsal 1 | Most proximal point of the 1st metatarsal, at the dorso-medial aspect at approx. 45° |
| | MT5B: base metatarsal 5 | Most proximal point of the 5th metatarsal, at the dorso-medial aspect at approx. 45° |
| | MT1: head metatarsal 1 | Most distal point of the 1st metatarsal, at the dorso-medial aspect at approx. 45°, next to the hallux tendon |
| | MT5: head metatarsal 5 | Most distal point of the 5th metatarsal, at the dorso-medial aspect at approx. 45° |
| | MT2B: base metatarsal 2 | Most proximal point of the 2nd metatarsal |
| | MT2: head metatarsal 2 | Most distal point of the 2nd metatarsal |
| Hallux | HLX: proximal phalanx | Most distal point of the proximal phalanx, at the dorso-medial aspect at approx. 45° |

## References

Schallig, W., Noort, J. C. van den, Piening, M., Streekstra, G. J., Maas, M., Krogt, M. M. van der, & Harlaar, J. (2022). The Amsterdam Foot Model: A clinically informed multi-segment foot model developed to minimize measurement errors in foot kinematics. *Journal of Foot and Ankle Research*, *15*, 46. https://doi.org/10.1186/s13047-022-00543-6

# C
# Decomposition of ground forces

The total GRFs were decomposed into four components, corresponding to the different foot segments in the musculoskeletal model (hindfoot, midfoot, forefoot and toes). Processing and calculation of the partial ground reaction forces (pGRF) was done using a custom program in MATLAB (R2017b), using the recorded motion, force and pressure data. The data was synchronised using either a hardware trigger (if available), or the timing of initial contact and toe-off. These gait events were detected using the method of Zeni et al. (2008).

The foot was divided into the aforementioned segments, based on a vertical projection of the foot markers (Giacomozzi et al., 2014). This was done as close as possible to the anatomical joint axes. The segment distributions are shown in Figure C.1. The CUB marker is not in the standard AFM markerset, so a virtual CUB marker was calculated at 2/3 of the distance between the PT and MT5B markers (closest to MT5B) (Deschamps et al., 2017). The hindfoot and midfoot were separated by a line through the TN and CUB markers. The midfoot and forefoot were separated by a line from MT1B to MT5B, through two virtual markers at the midpoints between MT1B and MT2B, and MT2B and MT5B, respectively. Finally, the forefoot and the toes were separated by a line parallel to the MT1-MT2-MT5 markers, but located more distally at 2/5 of the distance from MT1 to HLX. This distance was decided upon based on visual inspection.

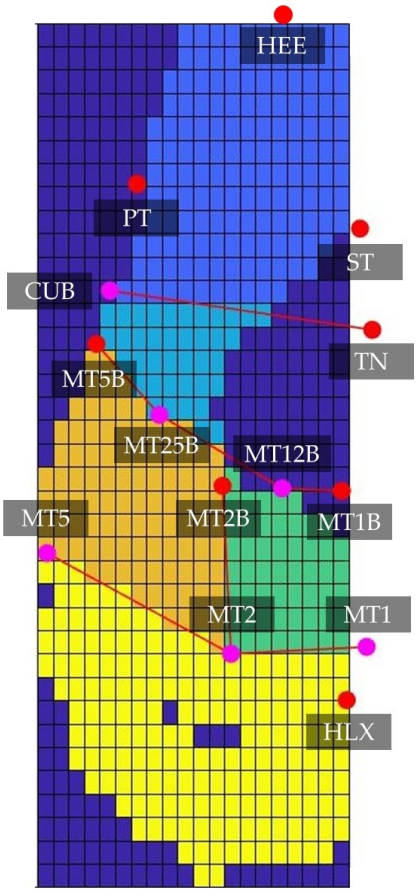


**Figure C.1:** Segment distributions of the foot model.

Based on this segmentation, all pressure sensors were assigned a segment label in the frame with maximum foot contact, i.e. the frame in which the footprint length is largest. These labels were then applied to the "active" sensors in each frame.

The vertical pGRFs per segment were calculated by summing the pressure of all sensors within a segment and multiplying by the surface of these sensors. The horizontal pGRFs were subsequently calculated using a proportionality scheme, meaning the total horizontal force was distributed pro-

portional to the ratio of the vertical force of that segment to the total vertical force (Saraswat et al., 2014):

$$F_{ML_i} = F_{ML}\left(\frac{F_{vertical_i}}{F_{vertical}}\right) \tag{C.1}$$

$$F_{AP_i} = F_{AP}\left(\frac{F_{vertical_i}}{F_{vertical}}\right) \tag{C.2}$$

with $F_{ML}$ the mediolateral horizontal force and $F_{AP}$ the anteroposterior horizontal force, for each segment $i$. The centers of pressure (COP) were calculated for each segment as well.

# References

Deschamps, K., Eerdekens, M., Desmet, D., Matricali, G. A., Wuite, S., & Staes, F. (2017). Estimation of foot joint kinetics in three and four segment foot models using an existing proportionality scheme: Application in paediatric barefoot walking. *Journal of Biomechanics*, *61*, 168–175. https://doi.org/10.1016/j.clinbiomech.2019.05.005

Giacomozzi, C., Leardini, A., & Caravaggi, P. (2014). Correlates between kinematics and baropodometric measurements for an integrated in-vivo assessment of the segmental foot function in gait. *Journal of Biomechanics*, *47*(11), 2654–2659. https://doi.org/10.1016/j.jbiomech.2014.05.014

Saraswat, P., MacWilliams, B. A., Davis, R. B., & D'Astous, J. L. (2014). Kinematics and kinetics of normal and planovalgus feet during walking. *Gait & Posture*, *39*(1), 339–345. https://doi.org/10.1016/j.gaitpost.2013.08.003

Zeni, J. A., Richards, J. G., & Higginson, J. S. (2008). Two simple methods for determining gait events during treadmill and overground walking using kinematic data. *Gait & Posture*, *27*(4), 710–714. https://doi.org/10.1016/j.gaitpost.2007.07.007

# D

# Inverse dynamics results

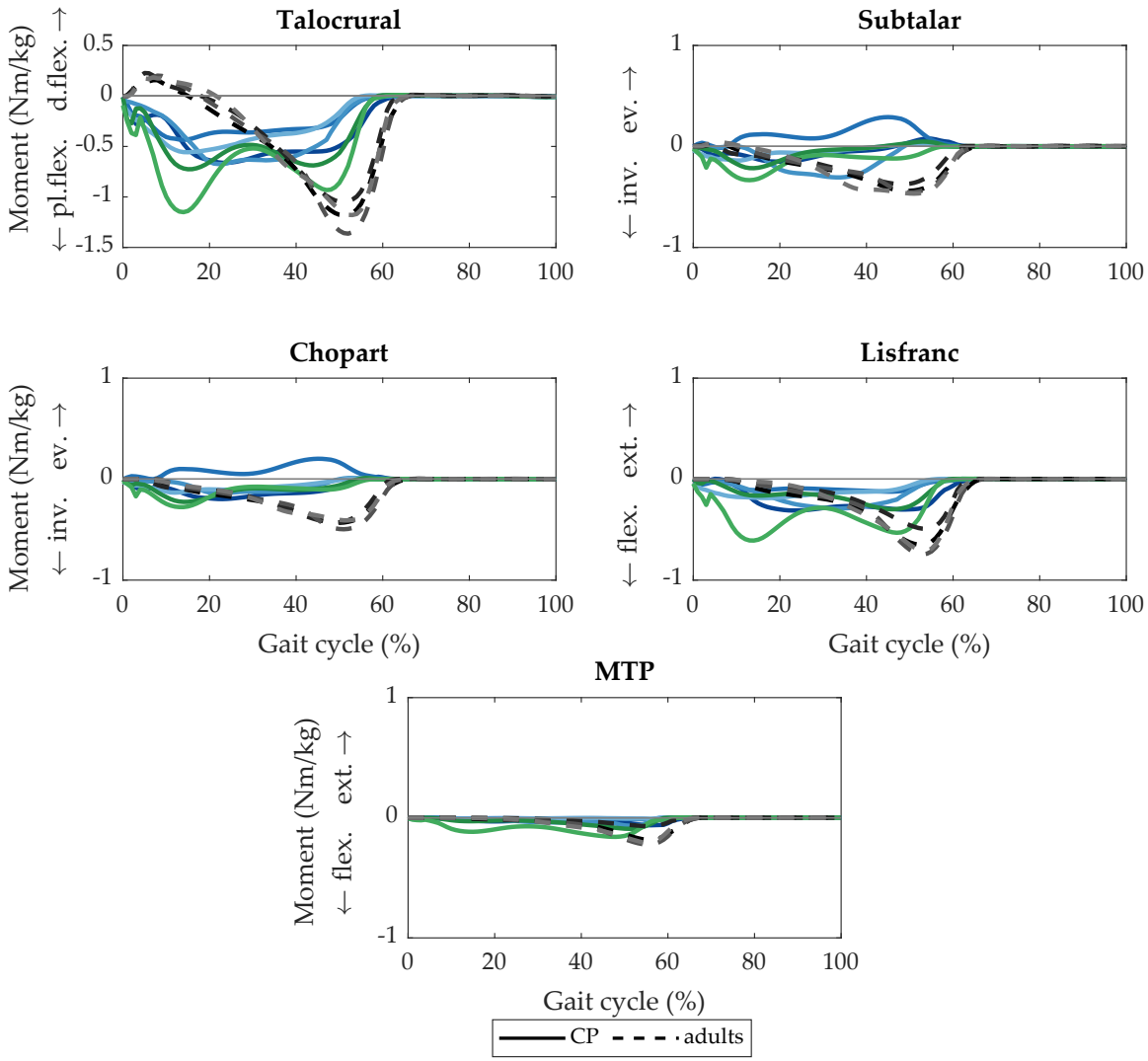


**Figure D.1:** Inverse dynamics results: foot joint moments per subject, averaged over three trials. Each line represents one subject. Children with a equinovarus deformity are represented with solid blue lines, while children with a cavovarus deformity are represented with solid green lines.